Kinematic and Moisture Characteristics of a Nonprecipitating Cold Front Observed during IHOP. Part II: Alongfront Structures

KATJA FRIEDRICH AND DAVID E. KINGSMILL

Cooperative Institute for Research in Environmental Sciences, University of Colorado at Boulder, and NOAA/Earth System Research Laboratory, Boulder, Colorado

CYRILLE FLAMANT

Service d'Aeronomie, Institut Pierre-Simon Laplace, Paris, France

HANNE V. MURPHEY AND ROGER M. WAKIMOTO*

Department of Atmospheric Sciences, University of California, Los Angeles, Los Angeles, California

(Manuscript received 28 August 2007, in final form 15 January 2008)

ABSTRACT

Kinematic and thermodynamic structures of a nonprecipitating cold front observed in west-central Kansas on 10 June 2002 during the International H_2O Project (IHOP) are examined with dropsondes and airborne instrumentation that includes Doppler radars, a differential absorption lidar, and in situ sensors. Intensive observations were collected along a 125-km segment of the front, with coverage of both the cold front leading edge and the post- and prefrontal areas. Whereas the first part of this two-part series of papers focused on across-front kinematic and moisture characteristics, the study herein investigates alongfront structures relevant for convection initiation. A northeast–southwest-oriented cold front moved into the observational domain from the northwest, but its motion slowed to less than 1 m s^{-1} in the early afternoon. In the late afternoon it was intersected by a north-northeast–south-southwest-oriented reflectivity thin line that was advected from the southwest, and another boundary that is an extension of a large-scale dryline paralleling the thin line but located farther to the east. Doppler wind synthesis suggests an increase in low-level horizontal wind shear across the cold front leading edge with the approach and intersection of the boundaries causing an increase in low-level convergence (up to $\sim 1 \times 10^{-3}$ s^{-1}), positive vertical vorticity (up to $\sim 0.5 \times 10^{-3}$ s^{-1}), and upward motion (up to ~ 1 m s^{-1}). An organized pattern of misocyclones (vertical vorticity maxima <4 km) and enhanced updrafts with a spacing of ~5–8 km were observed at the cold front leading edge. At the same time vortex lines manifested as horizontal vorticity maxima were observed within the cold air oriented perpendicular to the cold front leading edge and on top of the vertical wind shear layer. The analysis suggests that inflection point instability was the dominant mechanism for their development. Low Richardson number (0.3–0.4), short lifetime (<2 h), horizontal wavelength of 3–6 km, and collocation with strong horizontal and vertical wind shear are characteristics that support the hypothesis that these instabilities were Kelvin–Helmholtz waves. Towering cumulus developed along the cold front forming a convective cell close to the intersection of the cold front, dryline, and reflectivity thin line.

1. Introduction

Over the years many studies have focused on investigating processes that play a major role in cloud development and convection initiation along boundary layer convergence lines (also referred to as boundaries) for the purpose of improving storm forecasts and quantitative precipitation estimation. Large temporal variations of kinematic and moisture structures in the vertical and horizontal dimensions were found to make precise forecasts of when and where convection initiates along a boundary difficult. Many studies have demonstrated that the atmospheric conditions that favor deep cumulus cloud development vary considerably in time and space along the boundaries associated with their formation (e.g., Wilson et al. 1992; Crook and Moncrieff 1988; Ziegler et al. 2007).

An important mechanism for cloud development is

* Current affiliation: National Center of Atmospheric Research, Boulder, Colorado.

Corresponding author address: David E. Kingsmill, University of Colorado–CIRES, UCB 216, Boulder, CO 80309.
E-mail: david.kingsmill@colorado.edu

DOI: 10.1175/2008MWR2360.1

© 2008 American Meteorological Society

linked to horizontal and vertical shear instabilities across the boundary (e.g., Browning and Harrold 1970; Hobbs et al. 1980; Carbone 1982; Parsons and Hobbs 1983; Young and Johnson 1984; Wakimoto and Bosart 2000). Another important mechanism for cloud development is the collision of boundaries. In this context, many cases have focused on the interaction between frontal boundaries and drylines in the southern Great Plains (e.g., Bluestein and Parks 1983; Schaefer 1986; Bluestein et al. 1990; Hane et al. 1993; Parsons et al. 1991, 2000; Neiman and Wakimoto 1999; Weiss and Bluestein 2002).

Previous studies have examined fundamental processes for better understanding convection initiation but have often lacked detailed high-resolution measurements of moisture and kinematic structures prior to and during cloud development and convection initiation. Only recently has the linkage between horizontal shear instabilities and cloud development been examined with high-resolution measurements (Lee and Wilhelmson 1997a,b, 2000; Arnott et al. 2006; Geerts et al. 2006; Marquis et al. 2007). To fill this gap, the International H_2O Project (IHOP; Weckwerth et al. 2004; Weckwerth and Parsons 2006; Wilson and Roberts 2006) was conducted during May–June 2002 in the southern Great Plains. One of the aims of IHOP was to deduce processes relevant for convection initiation by using a dense network of high-resolution airborne and ground-based mobile observing systems. From the measurements collected on 24 May, Wakimoto et al. (2006) and Ziegler et al. (2007) were able to study cumulus formation and convection initiation near the intersection between a moving cold front and a dryline. They showed that no convection was initiated in this area, even though upward motions were relatively strong. Instead, cumulus cloud development was observed ~50 km to the east in an area with enhanced moisture and large potential instability. With the high-resolution mobile instrumentation used during IHOP, horizontal and vertical shear instabilities and moisture variations across drylines and cold fronts and their role in convection initiation have been intensively investigated (e.g., Arnott et al. 2006; Cai et al. 2006; Demoz et al. 2006; Geerts et al. 2006; Marquis et al. 2007; Murphey et al. 2006; Wakimoto et al. 2006; Weiss et al. 2006; Ziegler et al. 2007).

The datasets collected on 10 June 2002 during the IHOP experiment provide an opportunity to examine the kinematic and moisture structures of a nonprecipitating cold front and its interaction with two prefrontal boundaries in west-central Kansas (Fig. 1). This study is unique in that moisture and kinematic variations associated with horizontal and vertical shear instabilities along this cold front and with the intersection between the two boundaries are analyzed with a dense network of instruments. In contrast to many previous studies, observations were available over a wide spatial domain of up to ~100 km along and ~200 km across the cold front (Fig. 1, box A) prior to and during cloud development. Most of the previous studies analyzing processes that favor convection initiation along a cold front focused on the fast-moving, precipitating variety. With this analysis, we are able to investigate alongfront variations in the kinematic and moisture fields along a nonprecipitating cold front that slowed to less than 1 $m\,s^{-1}$ in the early afternoon. Across-front structures of the 10 June IHOP cold front were examined in Friedrich et al. (2007, hereinafter Part I) using ground-based and airborne instrumentation in the domain outlined as box A in Fig. 1, which includes in situ sensors, sounding systems, Doppler radars, a microwave radiometer, and a differential absorption lidar. Finescale (100 m and 90 s) structures of the 10 June cold front within a 20×20 km^2 domain (Fig. 1, box B) with an emphasis on misocyclones and cloud development were examined by Arnott et al. (2006). This paper focuses on the variability of kinematic and moisture structures observed along the front and in particular at the intersection between the cold front and prefrontal boundaries. The role of these structures in convection initiation will be discussed combining the findings of Arnott et al. (2006) and Part I, with additional observations over a wide spatial domain of up to ~100 km along the cold front. Section 2 provides a brief overview of the meteorological conditions for this case. Observing systems, including ground-based and airborne radar and lidar and in situ instruments, are described in section 3, while their analysis is presented in section 4. The influence of horizontal and vertical wind shear instabilities on cold-frontal structures are discussed in section 5. Conclusions are given in section 6.

2. Case overview

A more detailed case overview, including a description of synoptic conditions, evolution of the cold front, and thermodynamic structures, can be found in Arnott et al. (2006) and Part I. Some aspects relevant for the discussion of alongfront variability will be summarized in this section. During the analysis period between 1830 and 2100 UTC, the cold front was located in the northwestern part of the observing domain (Fig. 1, box A) and can be identified by a thin line of enhanced reflectivities (4–10 dBZ; Fig. 2). The cold front moved at a speed of less than 1 $m\,s^{-1}$ toward the southeast as revealed by the analysis of the Electra Doppler Radar

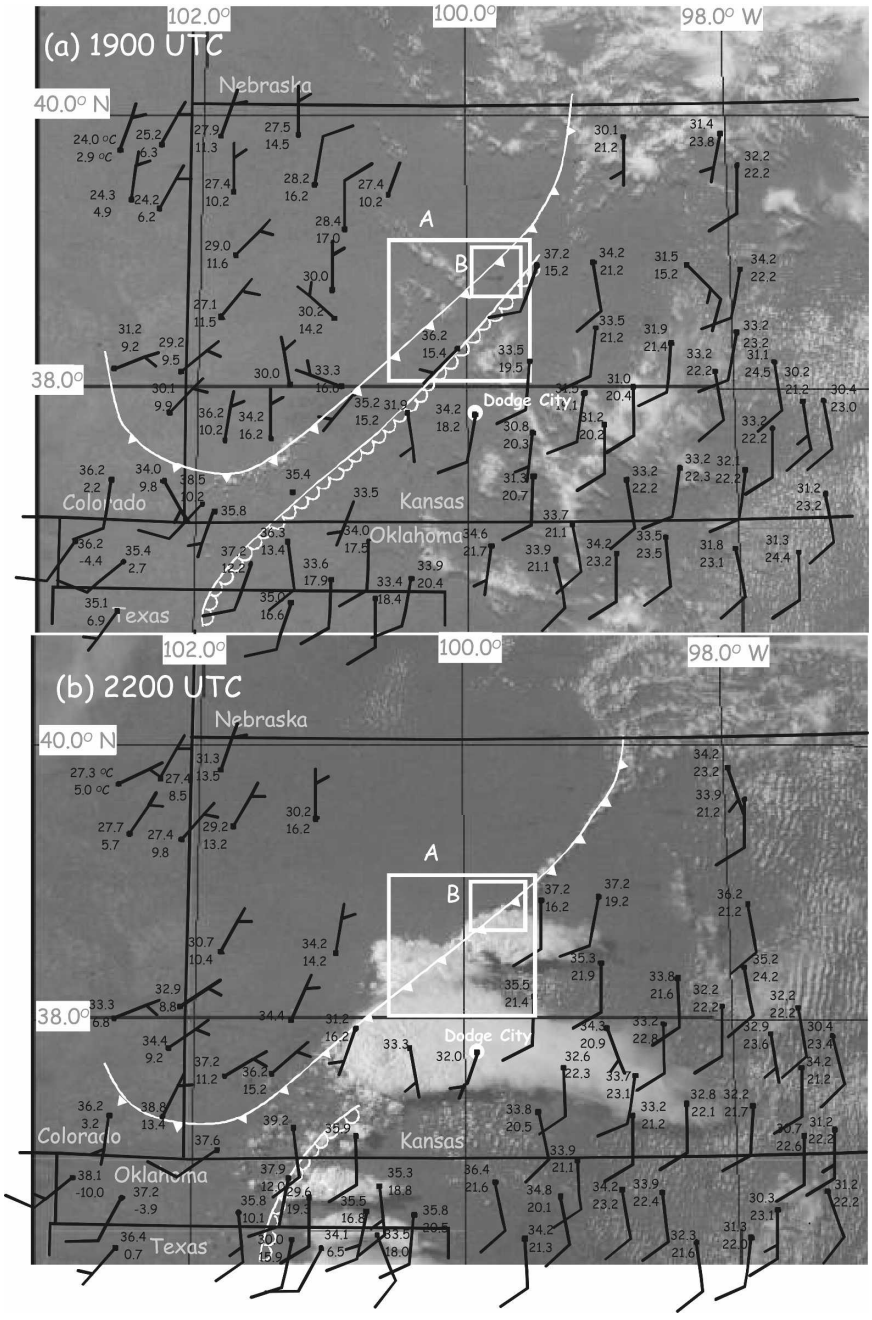

FIG. 1. Surface observations of wind (half barb: 2.5 m s^{-1} and full barb: 5 m s^{-1}), temperature (upper number; °C), and dewpoint temperature (lower number; °C) overlaid on *Geostationary Operational Environmental Satellite* (*GOES*)-*11* visible satellite image (1-km resolution) at (a) 1900 and (b) 2200 UTC. The location of the surface cold front is shown as a white line with alternating filled triangle symbols. The dryline is indicated as a white line with unfilled semicircles attached. The observational domain is located within the white box labeled as A; the observational domain used by Arnott et al. (2006) is located within the white box labeled as B. The location of the DDC WSR-88D is highlighted as a white circle.

(ELDORA) reflectivity and temperature from a mobile microwave radiometer (Part I). The deformation zone and horizontal convergence (frontogenetical processes) were observed during the entire analysis time, while the temperature gradient weakened during the afternoon (Arnott et al. 2006; Part I). Precipitation was not observed along the cold front within domain A during the 1800–2100 UTC analysis period. Analyses con-

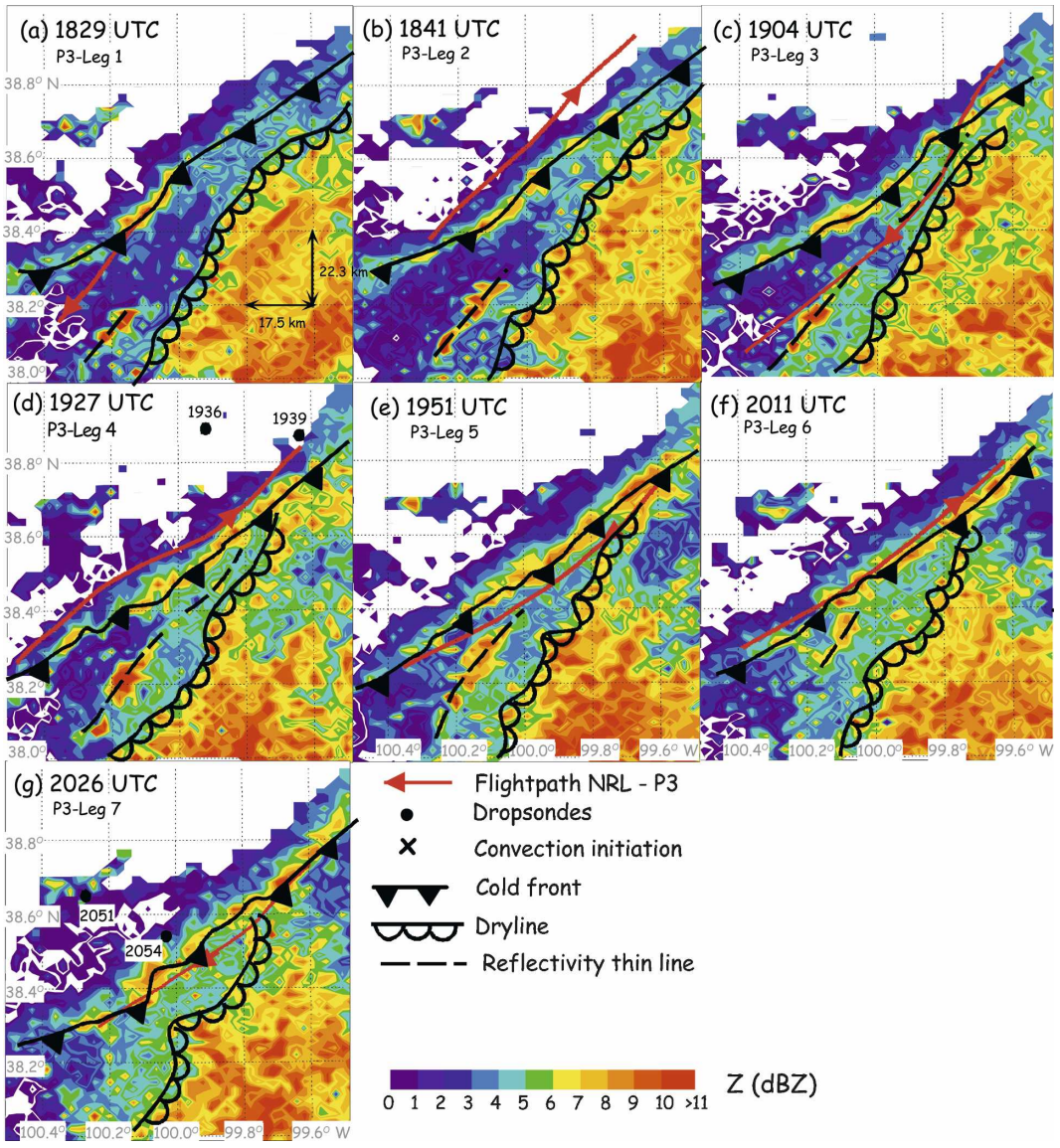

FIG. 2. Horizontal cross sections of color-coded DDC radar reflectivity (scale at the bottom) at 1.5 km MSL between 1829 and 2026 UTC. The flight path and direction of the NRL P3 aircraft are indicated as solid red lines with unidirectional arrows. (d) Locations of dropsondes deployed at 1936 and 1939 UTC are indicated by dots; (g) dropsondes released at 2051 and 2054 UTC are shown. The location of the surface cold front is shown as a black line with alternating filled triangle symbols attached. The dryline is indicated as black line with unfilled semicircles attached; (a)–(f) the reflectivity thin line is indicated as dashed black lines.

ducted in Part I showed evidence for certain gravity current characteristics at the cold front leading edge, such as Froude numbers between 0.7 and 1.4, a pronounced front-normal feeder flow toward the cold front leading edge, a rotor circulation, vertically elevated bulges in mixing ratio and radar reflectivity, reverse flow close to the ground, and pronounced updrafts. Wavelike flow on top of the cold air was observed in the early afternoon, becoming more pronounced in the late afternoon.

A second, more diffuse boundary was located to the southeast of the cold front. As shown in Part I this boundary developed through the interaction between the cold front and a large-scale dryline as described by Schultz (2004). Based on surface observations it was hypothesized that this boundary formed between 1200 and 1800 UTC and is an extension of the large-scale dryline located in the Oklahoma and Texas Panhandles. Within the IHOP observing domain, the boundary has characteristics of an elevated dryline,

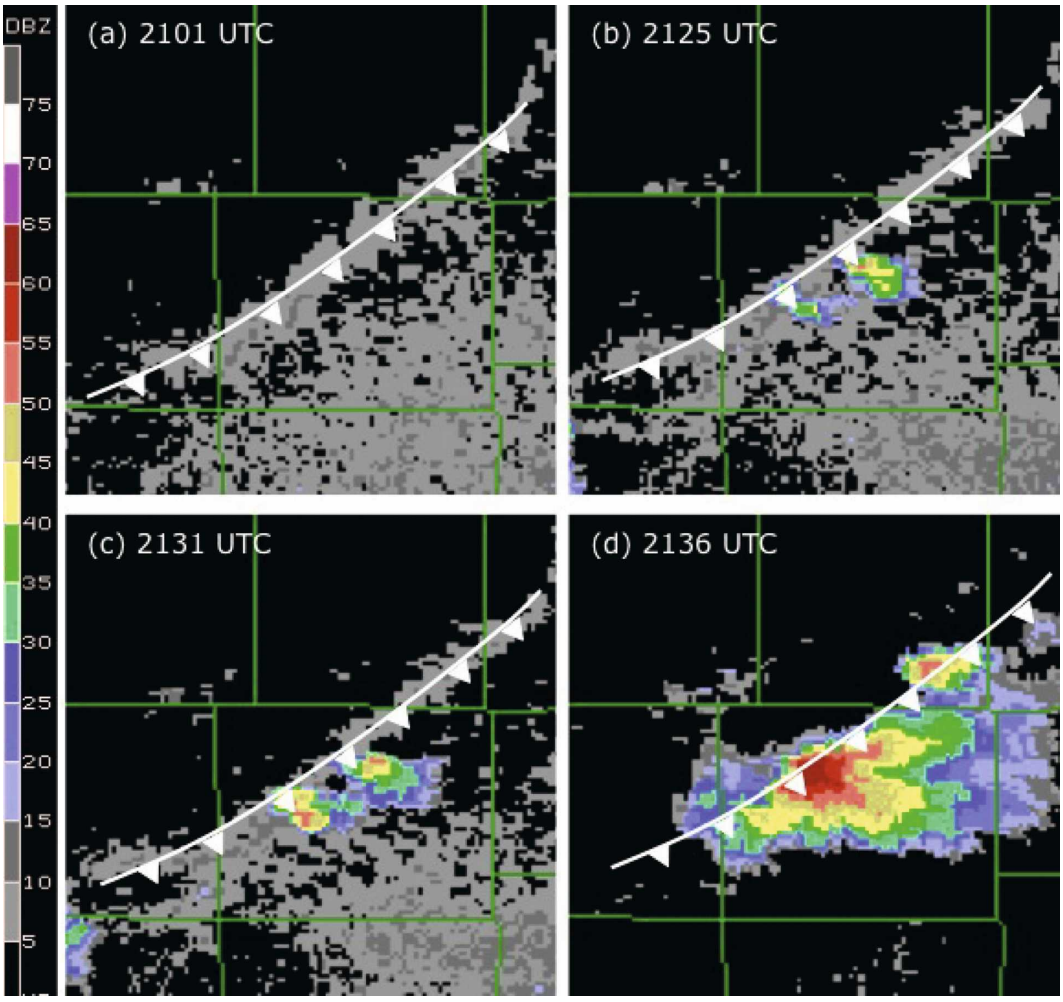

FIG. 3. Color-coded radar reflectivity (scale at the left) measured by the DDC WSR-88D at 0.5° elevation for (a) 2101, (b) 2125, (c) 2131, and (d) 2136 UTC within the observational domain (box A in Fig. 1). Plotting conventions for the cold front are the same as in Fig. 1. Green lines indicate county borders.

with horizontal gradients in mixing ratio (2 g kg^{-1} per 4 km at 1.2 km; Part I, Fig. 9) and wind restricted to the layer above the surface and below 1.5 km. The former characteristic of the diffuse, prefrontal boundary is different than a classical dryline, in which the hot air mass to its west is rather uniformly dry from the surface to the top of the deeply and strongly mixed boundary layer. Although the gradient in the mixing ratio across the dryline is smaller in the IHOP observing domain compared to that observed along the large-scale dryline (Fig. 1), a significant southwest-to-northeast gradient is still evident in this area (Part I). All subsequent references to the dryline in the IHOP observing domain refer to the eastern edge of this rather diffuse band of drier air concentrated in the middle of the prefrontal boundary layer, which should be understood as being distinctly different than a classical dryline.

Prefrontal dryline movement within the observing domain (Fig. 1, box A) was variable during the afternoon. In the southwestern part of the observational domain the dryline was almost stationary, but was characterized by small-scale eastward and westward displacements, or bulges (Fig. 2). In the northeastern part of the observational domain the dryline moved westward toward the cold front in the early afternoon, intersecting the cold front at ~1930 UTC. The intersection point between the cold front and dryline (hereafter referred to as the triple point) remained almost stationary throughout the afternoon. Although reflectivity increased by ~3 dBZ close to the triple point at 1951 UTC, deep convection did not initiate until 2136 UTC (Fig. 3). In their studies of the 24 May IHOP case, Wakimoto et al. (2006) and Ziegler et al. (2007) showed that deep convection is suppressed near the triple point

by a combination of stability, wind shear, weak vertical motion, and strong compensating downdrafts. Weiss and Bluestein (2002) presented a case in which the dryline was lifted by an approaching cold front at the triple point. In this case an intensified cloud development would be expected north of the triple point on 10 June. Satellite images (Fig. 1), radar reflectivity, and cloud development analysis of Arnott et al. (2006) on 10 June do not support this hypothesis.

Between the dryline and cold front within the hot, dry air mass, a line of enhanced reflectivity (5–10 dBZ) paralleling the dryline was observed moving toward the cold front between 1900 and 2015 UTC (Figs. 2a–f, dashed line). Several studies have observed similar multiple fine-line structures in radar reflectivity that were also manifested in gradients in moisture paralleling the primary dryline (e.g., Hane et al. 1993, 2001; Crawford and Bluestein 1997; Weiss et al. 2006). The multiple moisture gradients are referred to as secondary drylines. The moisture gradient related to the line of enhanced reflectivity on 10 June could not be characterized by the IHOP instrumentation because of their location farther to the northeast. Therefore, we will refer to this line simply as a reflectivity thin line. Its structure and relationship to convection initiation will be discussed in more detail throughout the paper. All three air masses were capped by a strong stable layer at 2–2.5 km (Part I, Figs. 4 and 5).

Later in the afternoon, between 2000 and 2200 UTC, the temperature gradient across the front weakened because of diabatic heating in the cloud-free cool air mass (Part I; Arnott et al. 2006). Dryline characteristics were still observed in the southwestern part of the observational domain, while they vanished almost completely in the northeastern part (Figs. 2f,g). At the cold front leading edge, low-level wind shear, low-level convergence, and vertical velocity increased (Part I). Analyses in Part I also showed that the mean updraft within the frontal convergence zone was deeper and more intense than earlier with mean magnitudes of $\sim$1 m s^{-1} and local maxima of $\sim$4 m s^{-1}. Thermodynamic conditions became more favorable for convection initiation later in the afternoon. Cumulonimbus clouds first developed along the cold front and the dryline outside of the observational domain in southwestern Kansas and the Oklahoma–Texas Panhandle at about 1930 UTC (Fig. 1). Analyses conducted in Part I showed that clouds form at and behind the cold front leading edge after 2030 UTC. Isolated reflectivity maxima (>35 dBZ), indicating the approximate location of convection initiation, were first observed at 2125 UTC by the Dodge City (DDC) Weather Surveillance Radar-1988 Doppler (WSR-88D) (Fig. 3) and the Doppler on Wheels (DOW; Arnott et al. 2006, Fig. 7f). The reflectivity maxima occurred close to the area where the cold front was intersected by the reflectivity thin line and the dryline (Figs. 2 and 3). IHOP observing systems discussed in this paper cannot be used to indicate the location of convection initiation because they were operated only until about 2100 UTC. Processes that intensified updrafts at the cold front leading edge prior to convection initiation will be discussed in more detail in sections 4 and 5.

3. IHOP observing systems and data processing

Alongfront kinematic and moisture structures were investigated by using data from instrumentation mounted on the Naval Research Laboratory (NRL) P3 aircraft that flew seven legs of $\sim$42–123-km length at $\sim$1.3 km MSL[1] ($\sim$0.6 km AGL). Figure 2 shows the DDC (location indicated in Fig. 1) WSR-88D reflectivity overlaid by the P3 flight track between 1829 and 2026 UTC. Four legs (P3 leg 1, leg 3, leg 5, leg 7) were primarily located in the prefrontal air mass, while the other three (P3 leg 2, leg 4, leg 6) were flown in the postfrontal air mass. The cold front was intersected at the northern part of the observational domain during P3 leg 3. Time periods of the airborne data used for further analysis are listed in Table 1. Also included in the analysis were vertical profiles of temperature, wind, and humidity with a resolution of 8 m from four global positioning system dropsondes (Vaisala model RD93) deployed from a Learjet at 1936, 1939, 2051, and 2054 UTC (Figs. 2d,g).

ELDORA provides reflectivity and pseudo-dual-Doppler-derived winds within a three-dimensional area around the cold front. These analyses extended horizontally up to $\sim$20 km on both sides of the aircraft and vertically from $\sim$1 to 4 km MSL. A detailed description of ELDORA is given by Hildebrand et al. (1994, 1996), and its configuration characteristics on 10 June 2002 are given in Table 4 of Part I. After the removal of noisy data and application of a fine-tuning navigation correction method (Bosart et al. 2002), the individual fore and aft scans were interpolated onto a three-dimensional Cartesian grid with a horizontal resolution of 600 m $\times$ 600 m and a vertical resolution of 250 m using a Cressman (1959) distance-dependent weighting scheme. The resolvable wavelength of motion is $\sim$3.6 km (Carbone et al. 1985). Wind components were derived using a dual-Doppler analysis from the fore and aft scans (Jor-

[1] In the following sections all heights will be expressed relative to mean sea level (MSL).

TABLE 1. List of the analyzed flight legs of the NRL P3 (P3): leg name, flight times, leg directional orientation, and length. Here, NE and SW indicate the northeast and southwest directions, respectively.

Name	P3 leg 1	P3 leg 2	P3 leg 3	P3 leg 4	P3 leg 5	P3 leg 6	P3 leg 7
Time (UTC)	1831–1837	1844–1856	1902–1920	1929–1944	1951–2005	2011–2023	2030–2041
Directional orientation	NE–SW	SW–NE	NE–SW	SW–NE	NE–SW	SW–NE	NE–SW
Length (km)	42	116	123	100	100	73	77

gensen et al. 1996). Kinematic structures and horizontal wind fields shown hereinafter are presented as front-relative quantities, assuming an average frontal speed of 0.9 m s^{-1} (Part I). The vertical velocities were derived by integrating the mass continuity equation up- and downward using a variational scheme (O'Brien 1970).

The water vapor Differential Absorption Lidar (DIAL) Lidar pour l'Etude des Interactions Aerosols Nuages Dynamique Rayonnement et du Cycle de l'Eau (LEANDRE) pointing in the horizontal direction was used to derive maps of the water vapor mixing ratio. More information on the instrument is given in Bruneau et al. (2001). LEANDRE configuration characteristics on 10 June 2002 are also provided in Table 4 of Part I. Water vapor mixing ratio was measured from 0.6 km out to a range of ~3 km from the lidar with an along-beam resolution of 300 m and an accuracy of ± 0.5 g kg^{-1} (Bruneau et al. 2001). Data were interpolated onto a two-dimensional Cartesian grid with a horizontal resolution of 450 m using a two-pass Barnes filter (Barnes 1973). Aircraft in situ measurements were also utilized for the flight tracks of the NRL P3 between 1830 and 2040 UTC. The data were recorded at a frequency of 1 Hz, and owing to the average P3 aircraft speed of ~115 m s^{-1}, the data have a spatial resolution ~115 m.

4. The observed alongfront variability

a. ELDORA analysis

Figure 4 shows the temporal evolution of ELDORA reflectivity and pseudo-dual-Doppler-derived winds between 1831 and 2041 UTC at 1.5 km MSL. The southwest–northeast-oriented cold front leading edge was indicated with reflectivities >2 dB*Z*. Analyses conducted in Part I showed that winds within the cool air sector were mainly ~2–4 m s^{-1} from the northwest at the surface backing to ~6–8 m s^{-1} from the southwest at 1.5 km MSL (~0.8 km AGL), as shown in Fig. 4. Further details regarding the temporal evolution of ELDORA reflectivity and kinematic structures across the cold front are presented in Part I. In the present paper, details related to horizontal and vertical wind shear across the cold front are discussed in section 5. Winds at 1.5 km in the northeastern part of the domain (<99.9°W) were primarily out of the south-southwest in both the post- and prefrontal air masses (Fig. 4). The variation in wind direction between the northeastern and southwestern parts of the observational domain is related to differences in kinematic boundary height, which is defined as the MSL height of the zero cold front–relative velocity. Although the kinematic boundary height does not necessarily coincide with the vertical gradient of temperature associated with the thermodynamic height of a boundary, it can serve as an approximate indicator and has been used for this purpose in numerous studies (e.g., Mueller and Carbone 1987; Carbone et al. 1990; Weckwerth and Wakimoto 1992; Atkins and Wakimoto 1997; Kingsmill and Crook 2003). The kinematic depths in these studies were often closely related to and somewhat smaller than independently measured thermodynamic depths. In our study, kinematic depth varied between ~1.0 and 1.25 km along the northeastern end of the cold front and between ~1.5 and 2.0 km along the southwestern end (Fig. 5). This suggests that the cold-frontal winds observed along the northeastern end were above the kinematic boundary in the area where the warm, moister air was lifted over the cold front leading edge.

Gradients in wind and radar reflectivity across the dryline were not clearly observed at 1.5 km by ELDORA because part of the dryline was located at the edge of the sampling domain (Fig. 4c) and the strongest gradients of wind and moisture occurred at and below 1.5 km. Part I showed that the wind gradient was only clearly evident at 0.9 km (Part I, Fig. 8d) and the moisture gradient, although most pronounced close to the surface, was still evident up to 1.5 km, but with weaker intensity (Part I, Fig. 9). During the afternoon the dryline approached the cold front leading edge, intersecting the front in the northeastern observational domain between 2000 and 2015 UTC (Figs. 2e,f and 4e,f). This area was well sampled by Arnott et al. (2006) using high-resolution reflectivity and Doppler velocity measurements. Their 23 km × 23 km wide observing domain is indicated as box B in Fig. 1 and at the top of Fig. 4. According to Arnott et al. (2006), who referred to the

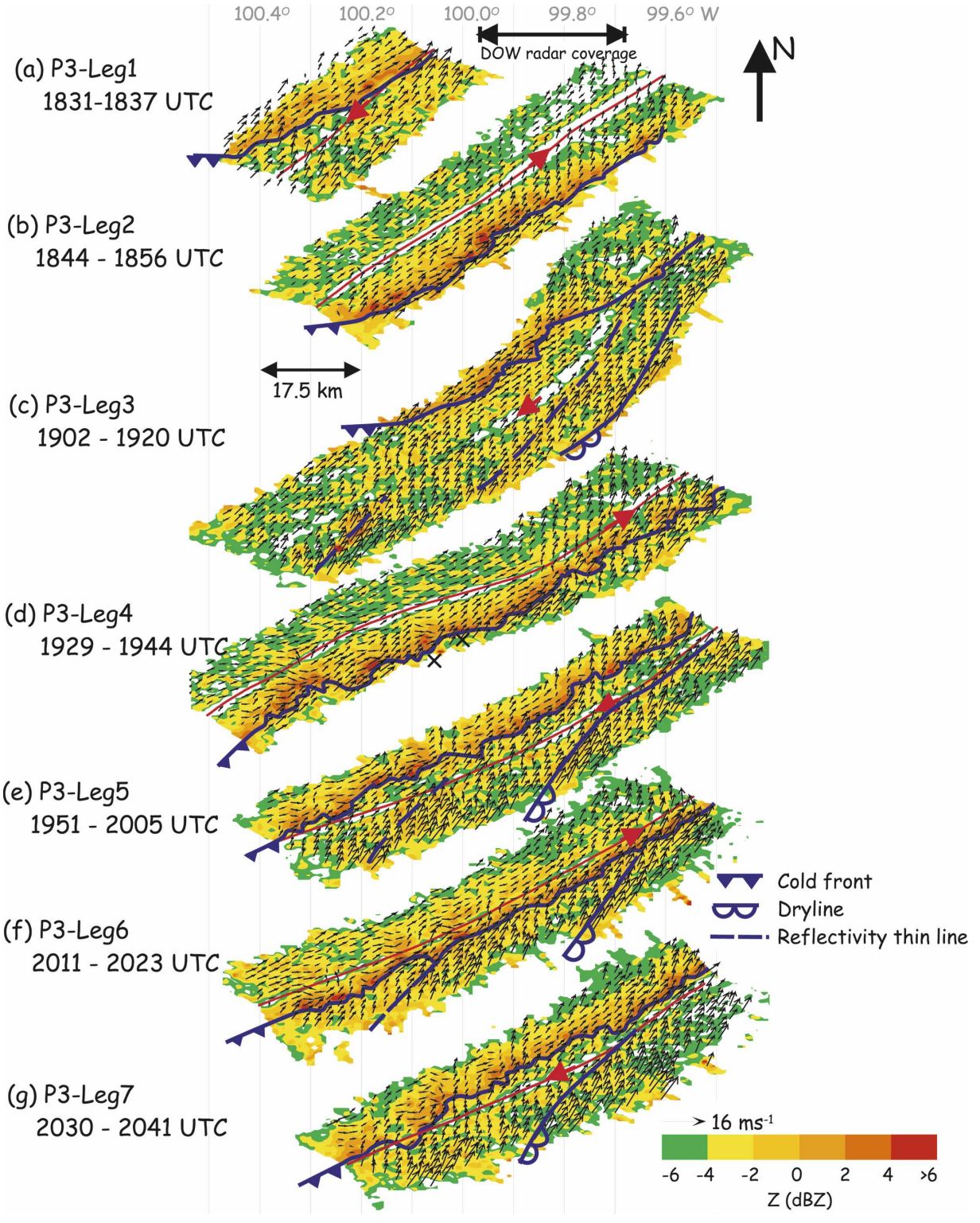

FIG. 4. Horizontal cross sections at 1.5 km MSL of ELDORA-derived dual-Doppler horizontal winds (arrows with scale indicated at bottom) and color-coded ELDORA reflectivity (scale at the bottom). Plotting convention for cold front and NRL P3 flight path are as in Fig. 2. (c), (e)–(g) The dryline is indicated as a blue line with two unfilled semicircles attached at the southwestern end; (c), (e), (f) reflectivity thin line is indicated as a dashed blue line. The DOW radar data coverage used in the study by Arnott et al. (2006) is indicated at the top of the figure labeled as DOW radar coverage.

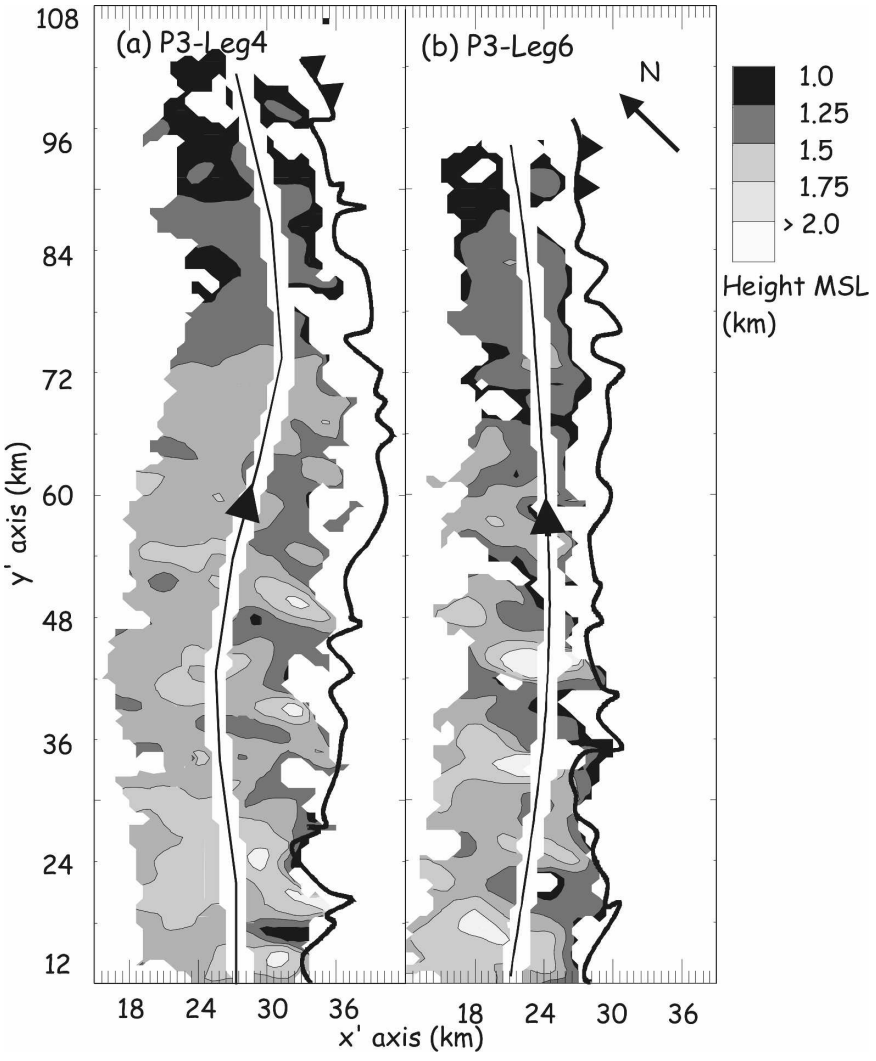

FIG. 5. Horizontal projection of kinematic boundary height (gray-shade scale at the top) for (a) P3 leg 4 executed from 1929 to 1944 UTC and (b) P3 leg 6 executed from 2011 to 2023 UTC. The location of the cold front leading edge is indicated as a thick black line with two filled triangles at its northeastern end. Flight path and direction of the NRL P3 is indicated as a thin black line with unidirectional arrows. The observational domain was rotated in a manner such that its y' axis is parallel to and its x' axis perpendicular to the cold front leading edge.

dryline as only a reflectivity thin line, the intersection between the dryline and cold front occurred between 2010 and 2020 UTC. Although they observed towering cumulus development along the entire length of the cold front at that time, no significant vertical velocity maxima were evident close to the triple point. Convective cells were first observed at 2136 UTC by the DDC radar in the vicinity of the triple point (Fig. 3d).

The hot, dry air mass between the cold front and the dryline was characterized by reflectivities of <0 dBZ and southwesterly winds of ~ 8 m s^{-1}. A prominent thin line of enhanced reflectivity (>-2 dB) was evident, consistent with the reflectivity thin line observed by the DDC radar (Fig. 2). Southwesterly wind speeds along this reflectivity feature were larger than in surrounding areas of the hot, dry air mass (Fig. 4). The reflectivity thin line was not a continuous feature, as indicated during P3 leg 3 (Fig. 4c) with a distinct break observed between 100.0° and 100.2°W. The northeastern extent of the reflectivity thin line with a maximum reflectivity of 2 dBZ and 10 m s^{-1} winds was only observed during P3 leg 3; during the next prefrontal flight leg (P3 leg 5, 1951–2005 UTC; Fig. 4e) the reflectivity thin line is only evident in the southwestern part of the domain. It is not

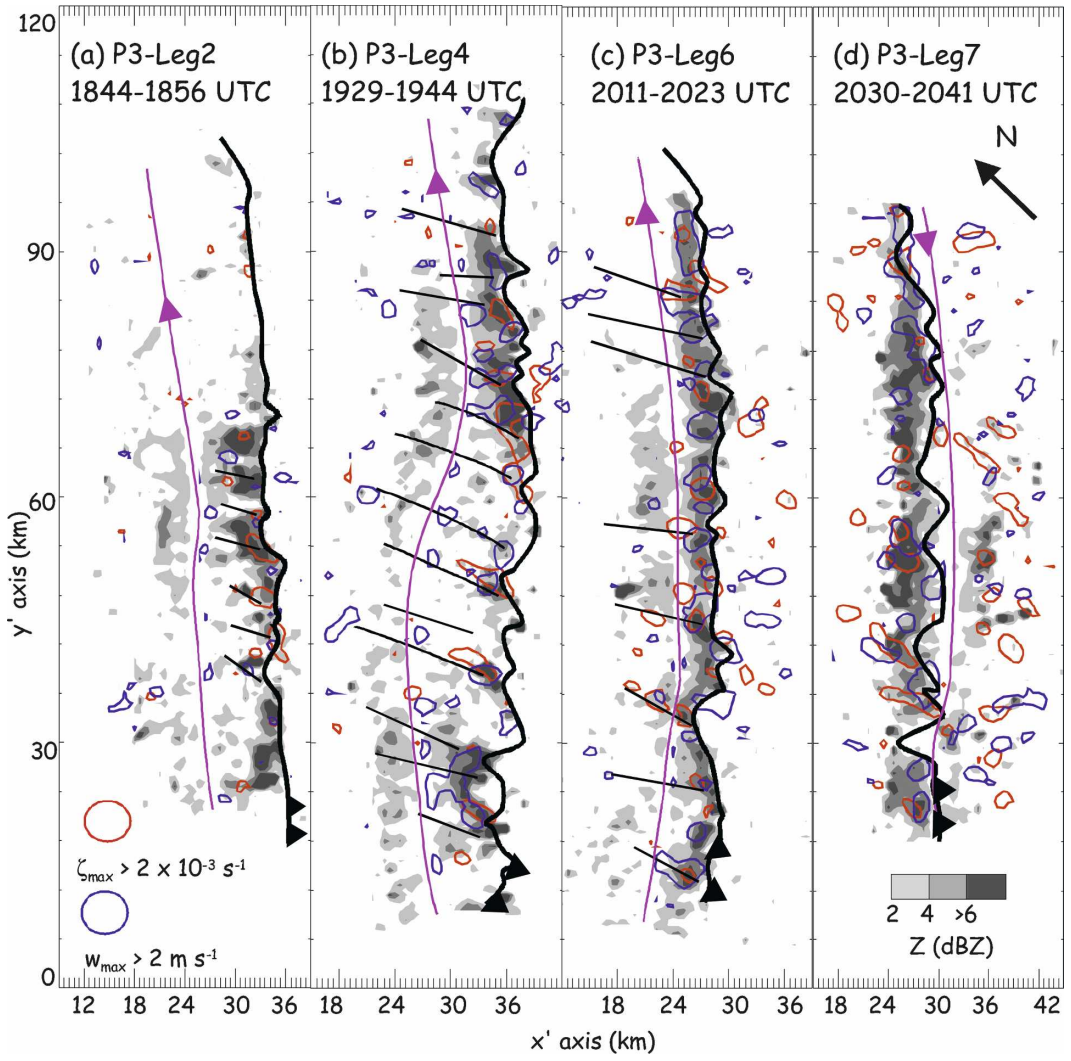

FIG. 6. Horizontal projection of maximum ELDORA reflectivity within the vertical column below 2.3-km height [gray-shade scale in (d)] overlaid by maximum vertical velocity [blue lines; scale in (a)], and maximum vertical vorticity [red lines; scale in (a)]. The location of the cold front leading edge is indicated by a thick black line with two triangles at its southwestern end. Flight path and direction of the NRL P3 is indicated by a magenta line with unidirectional arrows. (a)–(c) Locations of the vortex lines are indicated as thin black thin lines oriented 65° off the cold front leading edge. The observational domain was rotated in a manner such that its y' axis is parallel to and its x' axis perpendicular to the cold front.

clear whether the northeastern extent of the reflectivity thin line decayed or intersected the cold front. Arnott et al. (2006) did not observe the northeastern portion of the reflectivity thin line because their first analysis started at 1930 UTC. The southwestern extent of the reflectivity thin line, however, showed higher reflectivities (>6 dBZ) and stronger winds (12 m s^{-1}) than its northeastern counterpart. As the afternoon progressed, the southwestern extent of the reflectivity thin line approached and intersected the cold front between 2011 and 2023 UTC (Fig. 4f). Convective cells were first observed close to the location where the two boundaries intersected (Figs. 3 and 4). The southwestern extent of the reflectivity thin line was also not covered by Arnott et al. (2006) because it was located outside their observational domain.

In the early afternoon, the leading edge of the cold front was observed as an almost straight line of enhanced reflectivity with values of 0–6 dBZ (Figs. 4a–c). Core and gap structures were evident only in the southwestern part of the cold front and only weakly developed kinks in the reflectivity field were observed (Fig. 6a). Core and gap structures are areas of reflectivity maxima and minima along a boundary such as a cold

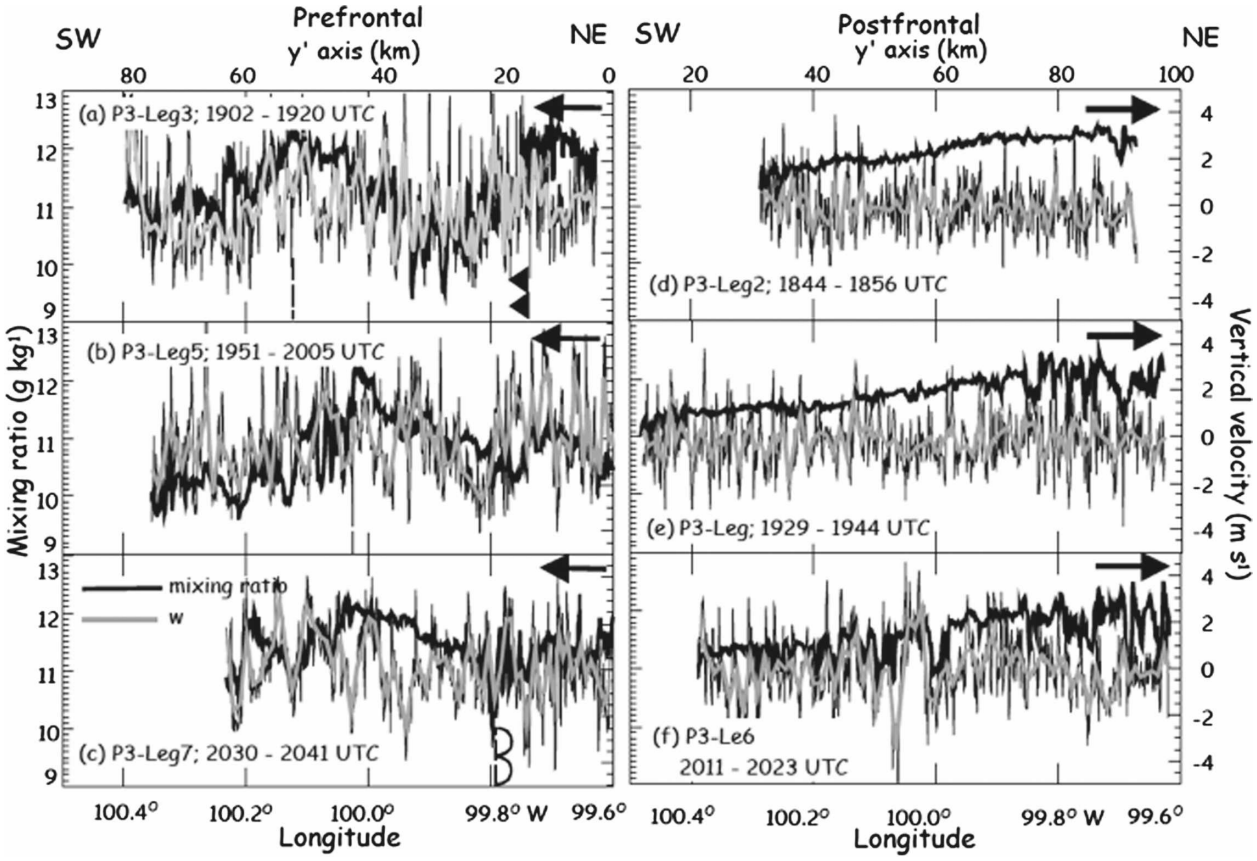

FIG. 7. Southwest–northeast horizontal profiles of equivalent potential temperature θ_e (black lines; see scale on the left) and virtual potential temperature θ_v (gray lines; see scale on the right) from the NRL P3 in situ instruments. The aircraft flew parallel to the cold front within the (a)–(c) prefrontal and (d)–(f) postfrontal area. Unidirectional arrows in the upper left corner in each panel indicate the direction of the NRL P3 aircraft. The approximate location of the flight track within the rotated coordinate system (Figs. 5 and 6) is indicated by the upper x axis denoted as the y' axis. The location of the cold front is indicated by two filled triangles in (a); the dryline is indicated by two unfilled semicircles in (c); and the reflectivity thin line is indicated as dashed line in (a) and (b).

front (Matejka et al. 1980; Hobbs and Persson 1982; Locatelli et al. 1995; Wakimoto and Bosart 2000; Jorgensen et al. 2003). These features are most commonly associated with precipitating boundaries, but also can occur with nonprecipitating boundaries. Figure 6 shows maximum values of reflectivity within a vertical column below 2.3-km height, an approach employed because the maxima occur at different analysis levels. As the afternoon progressed, inflections in the reflectivity field formed along the entire cold front with nonuniformly spaced reflectivity cores and gaps (Fig. 6b). After 2011 UTC, local reflectivity maxima and minima were separated almost uniformly by ~4 km along the entire cold front leading edge (Figs. 6c–d). The development of gap and core structures is often attributed to horizontal shear instabilities. Alternatively, they may develop as a consequence of the dynamics related to gravity currents when a high-density fluid overtakes a lower-density fluid (Matejka et al. 1980; Hobbs and Persson 1982). The types of observations collected on 10 June and their resolution might not be adequate to investigate this mechanism. However, our observations are capable of addressing the possible role of horizontal wind shear instabilities in modifying the cold front leading edge structure, a topic that will be discussed further in section 4.

b. NRL P3 in situ analysis

Spatial and temporal evolution of temperature, mixing ratio, and wind within the pre- and postfrontal air measured along the cold front are shown in Figs. 7–9. The alongfront, prefrontal in situ measurements clearly reveal the thermodynamic and kinematic characteristics of the three air masses (Figs. 7a–c, 8a–c, 9a–c). During P3 leg 3 the aircraft first intersected the cool, moist air in the northeastern part of the leg. This is indicated by the lowest θ_v values along the path (~316 K), mixing ratios of 11.5–12.5 g kg^{-1}, and southwesterly

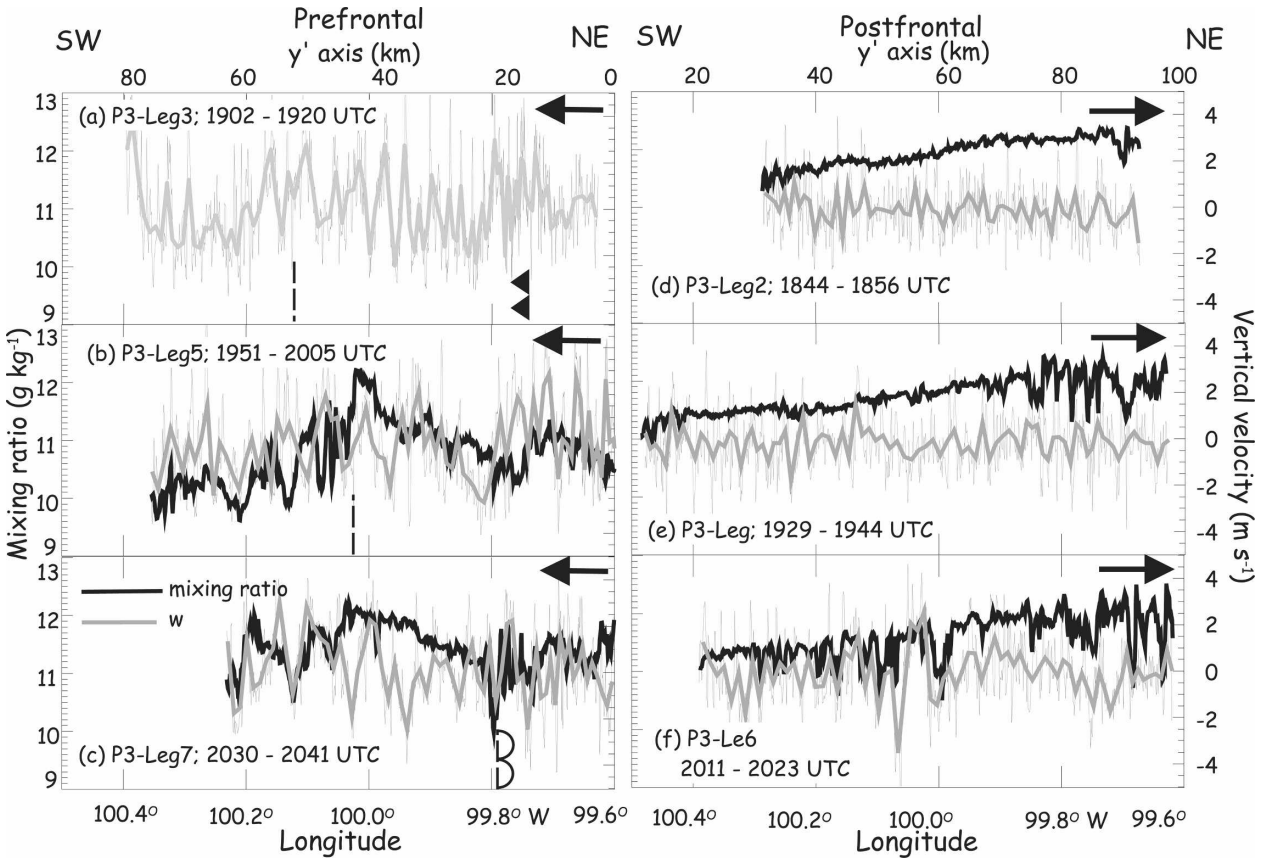

FIG. 8. As in Fig. 7, but horizontal profiles of mixing ratio (black lines; see scale on the left) and vertical velocity (gray lines; see scale on the right). Vertical velocity data were recorded at 1 Hz (thin gray lines) and averaged over 10 s (thick gray lines).

winds of ~4 m s^{-1}. The aircraft then traversed a slightly warmer ($\theta_v \sim 317$ K) and much drier ($q \sim 11$ g kg^{-1}, $\theta_e \sim 348$ K) air mass with winds of ~9 m s^{-1} from the south-southwest. This section was flown within the hot, dry air mass with the lowest q and θ_e values along the prefrontal flight legs and in the vicinity of the reflectivity thin line (Fig. 2c). The southwestern extent of the reflectivity thin line was intersected at ~100.15°W, showing an increase in θ_e up to ~354 K, $q \sim 12.5$ g kg^{-1}, and wind speed up to ~10 m s^{-1} from the southwest.

The P3 leg 5 was conducted entirely within the hot, dry air mass approaching only the dryline boundary at 99.6°–99.8°W. In this area winds increased slightly, the direction changed to more southerly, average mixing ratios were ~11 g kg^{-1}, and θ_e increased slightly. In situ measurements do not clearly indicate an intersection with the dryline. Another pronounced feature within the hot, dry air mass is the local maxima in θ_e and q collocated with a slight change in wind direction at ~100.05°W, which corresponds to the location of the southwestern extent of the reflectivity thin line (Fig. 2e). The southwestern part of the P3 leg 5 was slightly drier and warmer, with $\theta_e \sim 349$ K, $\theta_v \sim 318$ K, and $q \sim 10$ g kg^{-1} compared to the northeastern part, and winds of ~8 m s^{-1} were directed mainly from the southwest.

After 2030 UTC (P3 leg 7), the aircraft intersected the dryline between 99.7° and 99.8°W, which is indicated by a drop in θ_e of ~4 K and a decrease in wind speed from ~12 to ~8 m s^{-1}. Gradients in wind and moisture related to the reflectivity thin line were not observed (Figs. 7c, 8c, 9c). Between 1902 and 2041 UTC (Figs. 7a – c), the mean θ_v increased from 316 to 318 K, θ_e rose from 350 to 352 K, and the spatial variation of thermodynamic quantities within the prefrontal air decreased. The latter is indicated by a decrease in the standard deviation of θ_v from 1.7 (P3 leg 3) to 1.2 K (P3 leg 7), and θ_e from 0.5 to 0.3 K. The average mixing ratio within the hot, dry air increased from 10 to 12 g kg^{-1} between 1902 and 2041 UTC (Figs. 8a–c). The variation of vertical velocities ranging from −4 to 4 m s^{-1} did not change during this time in the prefrontal area (Figs. 8a–c).

Much less variation in thermodynamic and kinematic

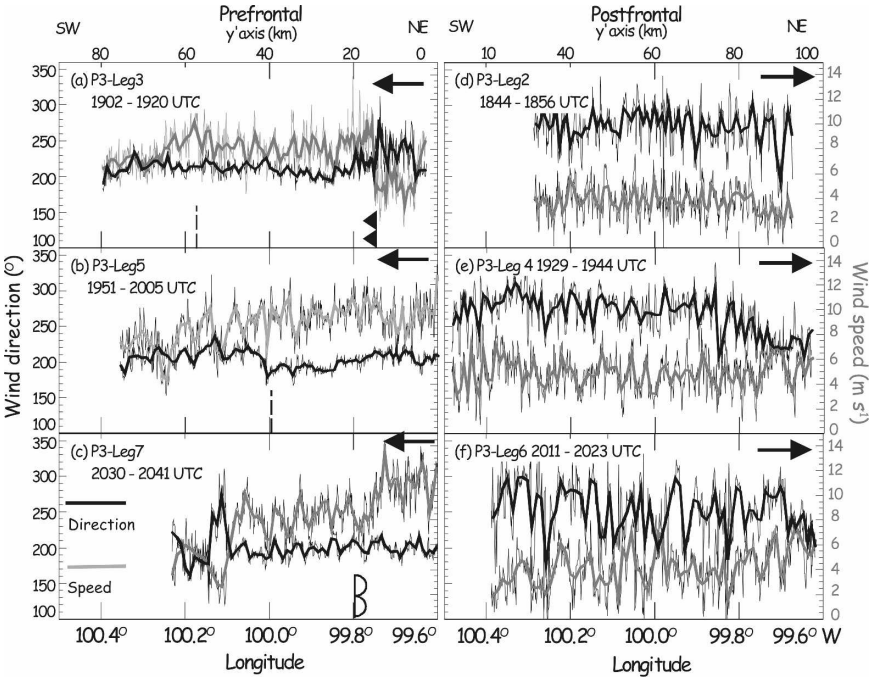

FIG. 9. As in Fig. 7, but horizontal profiles of wind direction (black lines; see scale on the left) and wind speed (gray lines; see scale on the right). Data were recorded at 1 Hz (thin gray and black lines) and averaged over 10 s (thick gray and black lines).

variables was observed within the postfrontal area (Figs. 7d–e, 8d–e, 9d–e). Mean θ_e showed a slight increase (from ~350 to ~351 K) between 1844 and 2023 UTC, and θ_v rose by ~3 K (from ~314 to ~317 K), which might be related to diabatic heating within the cloud-free cool air (Arnott et al. 2006). On the northeastern end of P3 leg 2 the aircraft flew away from the cold front toward cooler air, which is indicated by a θ_v decrease in Fig. 7d relative to Fig. 7e. Mixing ratio increased from ~11 to ~12.5 g kg^{-1} in moving from the southwestern to northeastern ends of the cold front (Figs. 8d–e). Interestingly, pronounced variations of up to ~2 K (1.5 g kg^{-1}) in θ_e and $\theta_v(q)$ were observed in the northeastern part during P3 leg 4, while θ_e and $\theta_v(q)$ varied only by ~1 K (0.5 g kg^{-1}) during P3 leg 2 and the southwestern part of P3 leg 4. It is most likely that these differences and the increase in q are linked to the variability of the kinematic boundary height (Fig. 5). In the northeastern part of the cold front, where the kinematic boundary height was <1.5 km, the P3 aircraft skimmed the top of the boundary where warm, moister air was lifted over the cool air. The flight track variations in θ_e and θ_v can likely be attributed to sampling this vertical interface between air masses where mixing should be enhanced. During P3 leg 6 the aircraft intersected an area with pronounced kinks in the reflectivity field (Fig. 2f). Here, θ_v increased up to ~318 K, the highest value observed within the postfrontal air mass. The winds were on average from the west at ~3.7 m s^{-1} during P3 leg 2 but shifted to west-southwesterly at ~4.2 m s^{-1} during P3 leg 6 (Fig. 9f). Variations in wind direction and speed increased significantly over time, as indicated by a rising standard deviation for wind direction from 29° to 42° and wind speed from 1.3 to 1.8 m s^{-1}. Vertical velocities during P3 leg 2 and leg 4 varied by ±2 m s^{-1}. Variance of the vertical velocity increased slightly up to ±3 m s^{-1} during P3 leg 6.

5. Influence of wind shear instabilities on cold-frontal structures

a. Horizontal wind shear

1) CHARACTERISTICS OF VERTICAL VORTICITY MAXIMA

Horizontal wind shear instabilities can trigger centers of small-scale (2–4 km) enhanced vertical vorticity, which we define as misocyclones. In the early afternoon (P3 leg 1–leg 3; 1831–1920 UTC), weak horizontal wind shear was present, with winds mainly from the southwest at 1.5 km MSL both in the post- and prefrontal area (Figs. 4a–c). The alongfront wind component differed mainly by ~2 m s^{-1} between the pre- and postfrontal air masses (Figs. 10a–c), and no misocyclones

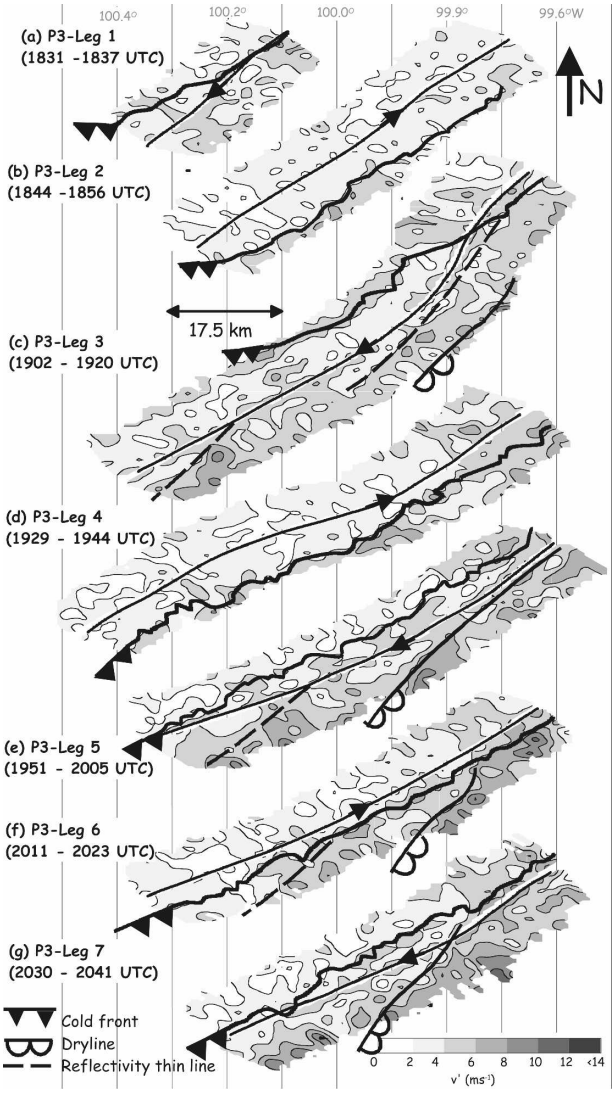

FIG. 10. Horizontal cross section at 1.5 km of the ELDORA-derived alongfront wind component (gray-shade scale at the bottom). Positive winds are from the south. Plotting conventions for cold front, dryline, reflectivity thin line, and NRL P3 flight path are as in Fig. 2.

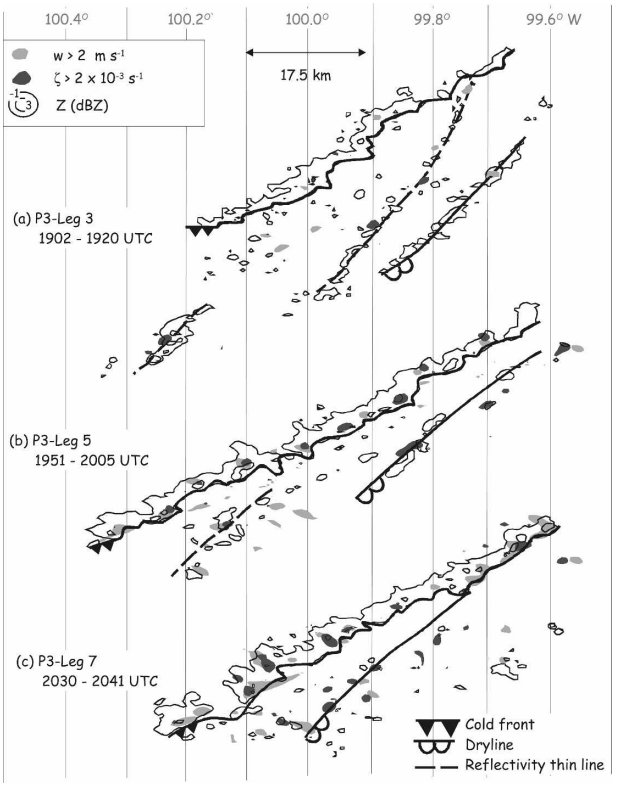

FIG. 11. Horizontal cross section at 1.5 km of ELDORA reflectivity indicated by the −1- and 3-dBZ contours (black lines), vertical velocity (areas with light-gray shading), and vertical vorticity (areas with dark-gray shading) for P3 (a) leg 3, (b) leg 5, and (c) leg 7. Plotting conventions for cold front, dryline, and reflectivity thin line are as in Fig. 2.

were observed (Fig. 11a). With the approach of the reflectivity thin line and dryline between 1920 and 2023 UTC (P3 leg 4–leg 6), horizontal wind shear across the cold front leading edge increased. The difference between alongfront winds in the post- and prefrontal air masses increased to 4–6 m s^{-1} (Figs. 10d–g) and during P3 leg 6 misocyclones with vertical vorticity magnitudes of $\zeta > 2 \times 10^{-3}$ s^{-1}, regularly spaced every 5–10 km, were observed (Fig. 11b).

Linear theory indicates that the fastest-growing mode will be at a wavelength of about 6 times the width of the wind shear zone (Miles and Howard 1964; Barcilon and Drazin 1972; Mueller and Carbone 1987), with a characteristic time of development of 100 s (Carbone 1983). Based on the 90-m-resolution University of Wyomning (UW) King Air flight-level data (Part I), the width of the wind shear zone across the cold front leading edge was about 1.7 km at 0.9 km MSL during 2006–2022 UTC. The resulting wavelength according to linear theory would be 10.2 km. ELDORA winds with coarser resolution reveal a slightly wider wind shear zone of 1.6–2.4 km at 1 km MSL during P3 leg 5 (1951–2005 UTC). The wavelength would be 9.6–14.4 km. The observed misocyclone spacing was about 5–8 km at 1.4 km MSL between 1946 and 2010 UTC based on the high-resolution DOW data (Arnott et al. 2006). ELDORA data reveal a misocyclone spacing of 5–10 km during P3 leg 6 at 1.5 km MSL (Fig. 11b). Although the development of these instabilities cannot be observed with the temporal resolution of the data, the observed wavelength of 5–10 km is in rough agreement with the 9.6–14.4-km wavelength derived from linear theory.

Matejka et al. (1980) and Friedrich et al. (2005) suggested that the difference between alongfront wind

components causes horizontal shear instabilities. The investigation of misocyclones along thunderstorm outflows by Friedrich et al. (2005) showed that a difference in alongfront wind components of >4 m s^{-1} was observed during those cases with the strongest misocyclones ($\zeta > 2.5 \times 10^{-3}$ s^{-1}). Comparing misocyclone organization during P3 leg 5 with leg 7 (Figs. 9b,c), the size of single misocyclones increased (99.9°–100.2°W), some misocyclones vanished (99.7°–99.9°W), and the organized pattern disappeared. Although misocyclones are not equally spaced in the horizontal projection of maximum vertical vorticity within a vertical column in Fig. 6, the number and size of misocyclones increased from P3 leg 4 to leg 6 and slightly decreased from P3 leg 6 to leg 7 (red circles in Fig. 6c,d). Arnott et al. (2006) and Marquis et al. (2007) were able to track several misocyclones during their lifetime based on high-resolution radar data observed on 10 June. They observed that after 2020 UTC several misocyclones began to merge.

2) Effects of misocyclones on kinematic and moisture field

Several studies have shown that core and gap structures can develop along boundaries from horizontal shear instabilities (e.g., Hobbs et al. 1980; Wakimoto and Bosart 2000). More recent investigations have also demonstrated that misocyclones can distort the horizontal wind field by producing local maxima of low-level convergence (e.g., Kingsmill 1995; Lee and Wilhelmson 1997a,b; Friedrich et al. 2005; Arnott et al. 2006; Marquis et al. 2007). The locations of enhanced low-level convergence are associated with enhanced upward motions, and therefore preferred regions to form reflectivity cores. Arnott et al. (2006) and Marquis et al. (2007) used high-resolution radar data to show the development of several significant kinks in the reflectivity resulting from misocyclones that are collocated with areas of strong updraft. Radar reflectivity measured by ELDORA also reveals kinks and distinct reflectivity cores separated by reflectivity gaps during the existence of misocyclones after about 1900 UTC (Figs. 2, 4, and 6). The evolution of upward motion followed a trend similar to the misocyclones' life cycle. The number of vertical velocity maxima increased after 1930 UTC, as is evident by comparing P3 leg 2 with leg 4 in Fig. 6 and P3 leg 3 with leg 5 in Fig. 11. After 2023 UTC the trend reversed with the number of vertical velocity maxima decreasing as indicated by comparison of P3 leg 6 with leg 7 in Fig. 6 and P3 leg 5 with leg 7 in Fig. 11. The vertical velocity maxima were mainly adjacent to the reflectivity cores and located southwest of the misocyclones during P3 leg 4 (Fig. 6b) and leg 5 (Fig. 11b). This typical pattern of misocyclones and vertical velocity maxima was also noted in other studies (e.g., Carbone 1983; Mueller and Carbone 1987; Kingsmill 1995; Lee and Wilhelmson 1997a; Friedrich et al. 2005; Murphey et al. 2006; Arnott et al. 2006; Marquis et al. 2007).

Murphey et al. (2006) showed that the interaction between misocyclones and the moisture field along a north–south-oriented dryline was highly variable in time. They observed areas of moisture advection collocated with misocyclones, moisture advection toward the west side of the dryline north of misocyclones, and drier air advection toward the east side of the dryline south of misocyclones. Similar results on the effects of misocyclones on the moisture field along boundaries have also been reported by Pietrycha and Rasmussen (2004), Buban et al. (2007), and Marquis et al. (2007). To investigate the influence of misocyclones on the moisture distribution on 10 June, mixing ratios derived from LEANDRE-II measurements are superimposed on ELDORA-derived dual-Doppler horizontal winds (Fig. 12). Because the collection of lidar data was limited to a range of ~3 km from the flight track, aircraft navigation made it difficult to capture parts the cold front and misocyclones. The moisture distribution along the cold front was only well captured within P3 leg 6, while the moisture field ahead of the cold front was only well observed during P3 leg 7. Generally, LEANDRE-II-derived mixing ratios exhibited only a small degree of horizontal heterogeneity along the indicated swath. Mixing ratios at 1.5 km MSL were ~4 g kg^{-1} higher along the northeastern end of the cold front compared to the southwestern end during P3 leg 6 (Fig. 12a), which might be related to alongfront variabilities in the kinematic boundary height (Fig. 5) and prefrontal mixing ratio (Figs. 8d–f). LEANDRE measurements at 1.5 km along the southwestern end of the cold front were still located within the cool, moist air. Higher mixing ratios observed by LEANDRE along the northeastern end of the cold front correspond to an area where the warm, moister air was transported upward and over the cool air resulting from the lower kinematic boundary heights relative to the southwestern part. Moisture variations of up to 3 g kg^{-1} were observed ahead of the cold front (Fig. 12b) during P3 leg 7, with higher values close to the area of convection initiation between 100.0° and 100.1°W. No linkage between the horizontal distribution of mixing ratio, vertical velocity, and vertical vorticity was observed during P3 leg 6 (Figs. 12c,d). Phenomena reported by Murphey et al. (2006) might have been missed either because of their high temporal variation or because they are not as evident as in the Murphey et al. study because of the

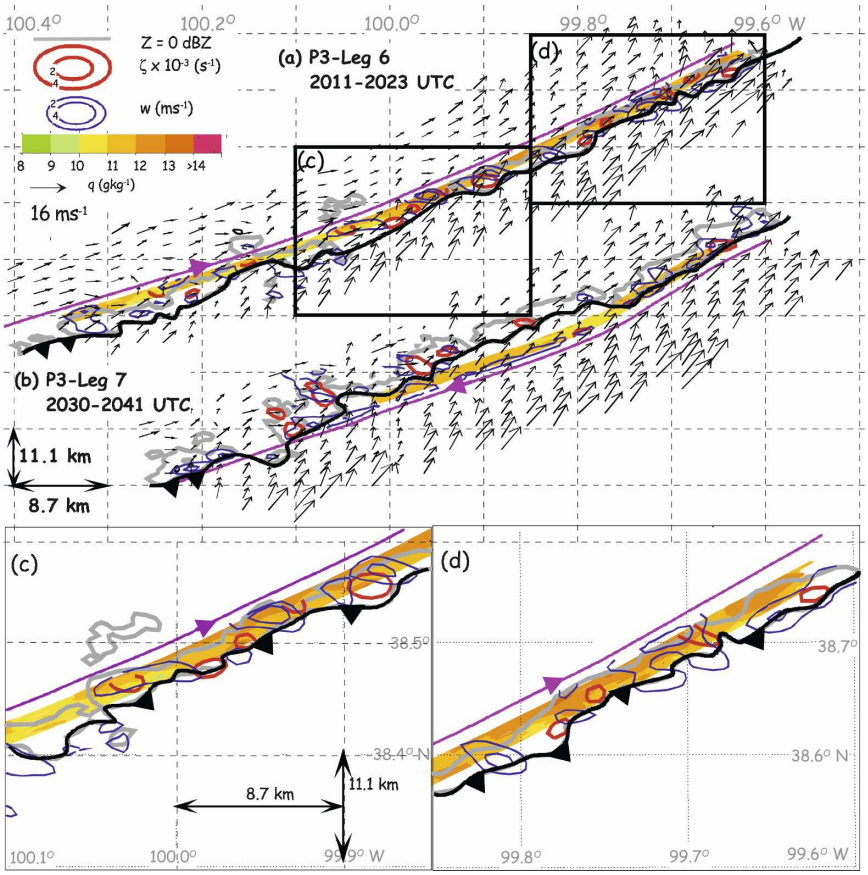

FIG. 12. Horizontal cross section at 1.5 km MSL of color-coded LEANDRE-II mixing ratio [scale at the top of (a)] overlaid by vertical velocity contours [blue lines; scale at the top of (a)], vertical vorticity contours [red lines; scale at the top of (a)], and the 0-dB*Z* reflectivity contour (gray lines) derived from ELDORA measurements. Plotting convention for cold front and NRL P3 flight path are as in Fig. 2. (a), (b) ELDORA-derived dual-Doppler horizontal winds [arrow with scale indicated at the top of panel (a)] are overlaid. (c), (d) Zoom-in of sections highlighted in (a).

lower mixing ratio gradient between cool, moist and warm, moister air on 10 June.

b. Vertical wind shear

1) CHARACTERISTICS OF HORIZONTAL VORTICITY MAXIMA

Linearly structured horizontal vorticity maxima (vortex lines) were observed behind and almost perpendicular to the cold front leading edge between 1930 and 2045 UTC. These structures were also evident as undulation in kinematic boundary height (Fig. 5) and to some extent in the horizontal wind field (Figs. 4d–g). Representative positions of the vortex lines are shown as blue lines in Fig. 13. The identification of those lines, based primarily on the magnitude of maximum horizontal vorticity (Fig. 13) and secondarily on kinematic boundary height (Fig. 5), was particularly difficult because the vortex lines were transient. The vortex lines were first observed in the cool air within ~12 km of the cold front leading edge at 1844–1856 UTC (P3 leg 4; Fig. 13a), but extended out to ~20 km behind the cold front between 1929 and 1944 UTC (P3 leg 4; Fig. 13b). Vortex lines are fewer in number and are spaced farther apart between 2011 and 2023 UTC (P3 leg 6; Fig. 13c). The lines were oriented from the north-northwest to south-southeast at an angle of ~65° relative to the cold front. Between 1929 and 1944 UTC (P3 leg 4), the observed features were spaced horizontally at 3–6-km intervals and were aligned almost perpendicular to the boundary layer wind and almost parallel to the vertical wind shear vector (Fig. 13b). The wind shear vector was derived between 2.55 km MSL and the lowest analysis level, located at 1.05 km. During the analysis period the

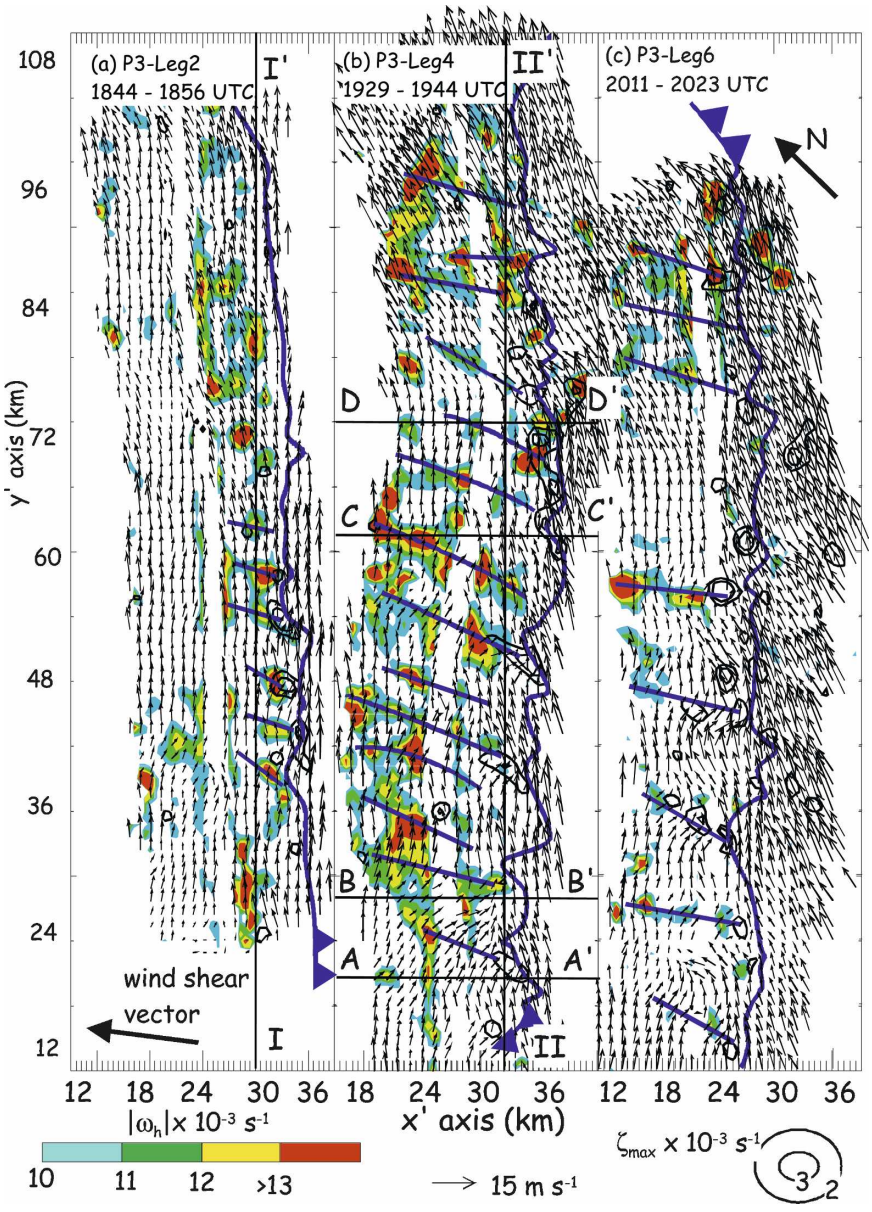

FIG. 13. Horizontal projections of ELDORA-derived dual-Doppler data for P3 (a) leg 2, (b) leg 4, and (c) leg 6. Color-coded maximum horizontal vorticity contours (scale at the bottom) are overlaid by maximum vertical vorticity contours (black lines) and horizontal wind vectors at 1.5 km (arrows with scale indicated at the bottom). (a) Mean wind shear vector between 1.05- and 2.55-km height during 1844–2023 UTC is shown. The location of the cold front leading edge is indicated by the vertically oriented blue line. The location of the vortex lines is indicated by blue lines oriented almost perpendicular to the cold front leading edge. Vertical black lines indicate alongfront vertical cross sections from (a) I–I′ and (b) II–II′ shown in Fig. 14; horizontal black lines in (b) indicate the across-front vertical cross sections A–A′, B–B′, C–C′, and D–D′ shown in Fig. 15. The observational domain was rotated in a manner such that its y' axis is parallel and its x' axis perpendicular to the cold front.

wind shear vector behind the cold front was primarily directed toward the northwest (~80° off the cold front). The displacement of the vortex lines could not be tracked because of the coarse temporal resolution (~40 min) of the ELDORA data between the postfrontal flight legs. Arnott et al. (2006) also observed these vortex lines between 1930 and 2000 UTC, which were indicated by reflectivity and convergence maxima. They

determined that the lines traveled at a speed of ~9.6 m s^{-1} toward the north-northeast and had a horizontal spacing of ~3 km. Because they could not diagnose the origin of these lines they referred to them as linear reflectivity maxima.

2) BOUNDARY LAYER HORIZONTAL ROLLS

One hypothesis for the origin of these organized structures is boundary layer horizontal rolls. Horizontal convective rolls are counterrotating horizontal vortices that can be forced by thermal and/or dynamic instabilities (e.g., Lilly 1966; Brown 1980; Stensrud and Shirer 1988; Weckwerth et al. 1997). With thermal instability, the roll energy is obtained from buoyancy while wind shear organizes the clouds into bands. Although the UW King Air data reveal that the cool air mass was neutrally stratified (Part I, Fig. 7), it is plausible that the environment could become slightly unstable in the afternoon resulting from the diabatic heating within the cloud-free cool air. In this section, environmental conditions on 10 June will be examined to determine if boundary layer horizontal convective roll formation is favored from a theoretical standpoint, and, if so, whether their characteristics are consistent with the observed characteristics of the vortex lines (wavelength, diameter, location, up- and downdraft pattern).

Because pronounced vertical wind shear was observed between the cold-frontal outflow and the upstream flow on 10 June (Part I), it is more likely that the dominant mechanism associated with the development of horizontal convective rolls was related to dynamic instabilities. Dynamic instabilities include parallel instability in which the roll energy is obtained either from along-roll shear or inflection point instability, which forms rolls when the wind profile has an inflection point in the cross-roll direction. Numerical simulations indicate that roll orientation changes from being parallel to the mean wind shear vector for parallel instabilities to perpendicular for inflection point instabilities (Stensrud and Shirer 1988). On 10 June the vortex lines were aligned with the wind shear vector, almost perpendicular to the mean boundary layer wind. Vertical wind profiles within the postfrontal region revealed a strong directional wind shear component (vertical profiles of the horizontal wind are shown in Part I, Figs. 5, 6, and 8), so it is more likely that inflection point instability was the dominant mechanism. Observational studies show that roll orientation is governed by vertical wind shear when the shear has a strong directional component (e.g., Ferrare et al. 1991; Arnott et al. 2006; Ziegler et al. 2007). In the observational studies that have strong speed shear, horizontal convective rolls were mainly aligned with the mean wind (e.g., Weckwerth and Wakimoto 1992).

The rolls typically have a wavelength of about 2–4 times the boundary layer depth. With a boundary layer depth of ~0.6 km (Part I), a horizontal separation of ~1.2–2.4 km would be expected, which cannot be resolved with the ELDORA data having a resolvable wavelength of 3.6 km. High-resolution radar data from 10 June with a resolvable wavelength of 1.2 km presented by Arnott et al. (2006) derived a spacing of 3 km, which is too coarse for horizontal convective rolls. Theory also suggests that the diameter of each roll has a spatial scale that is of the same order as the boundary layer depth. The only measure of diameter in the present case comes from the maxima of horizontal vorticity shown in the vertical cross section in Figs. 14 and 15. The vortices seem to be elevated and located close to the shear layer, which does not support the existence of horizontal convective rolls. Figure 16 shows vertical velocity and mixing ratio within the northern cool air sector ($80 < y' < 96$ km in Fig. 13c; Fig. 8f) during P3 leg 6. The aircraft flew close to the leading edge at 1.3 km MSL, which is also close to the kinematic boundary. The mixing ratio was generally well correlated with vertical velocity, showing increasing values in the updraft region when moister air is transported upward and vice versa. Nevertheless, a pronounced pattern of updrafts and downdrafts spaced at ~2-km intervals indicating counterrotating vortices were not observed.

3) KELVIN–HELMHOLTZ INSTABILITIES

Inflection point instability is also viewed as a generalized Kelvin–Helmholtz-type instability (Brown 1980; Stensrud and Shirer 1988; Ziegler et al. 2007). Kelvin–Helmholtz waves occur at the interface between two flows of different wind velocity and density when strong vertical wind shear and low Richardson numbers are present. Strong vertical shear of the horizontal wind occurred close to the kinematic boundary on 10 June, which separates the cold outflow moving toward and the upstream flow moving away from the cold front leading edge (Fig. 15). The front-normal wind shear derived from dropsonde data (Part I) varied between 0.01 and 0.02 s^{-1} (Table 2). Mueller and Carbone (1987) observed vertical wind shear of 0.009–0.02 s^{-1} in the vicinity of Kelvin–Helmholtz waves, which were observed by ground-based radar on top of a thunderstorm outflow. On 10 June, the wind shear zone was located between ~1.5 and 2.5 km MSL (Fig. 15).

Kelvin–Helmholtz waves develop when the Richardson number is below 0.25 and maintain when it is less than 1.0 (Miles and Howard 1964). On 10 June 2002, the Richardson number provides the strongest evidence

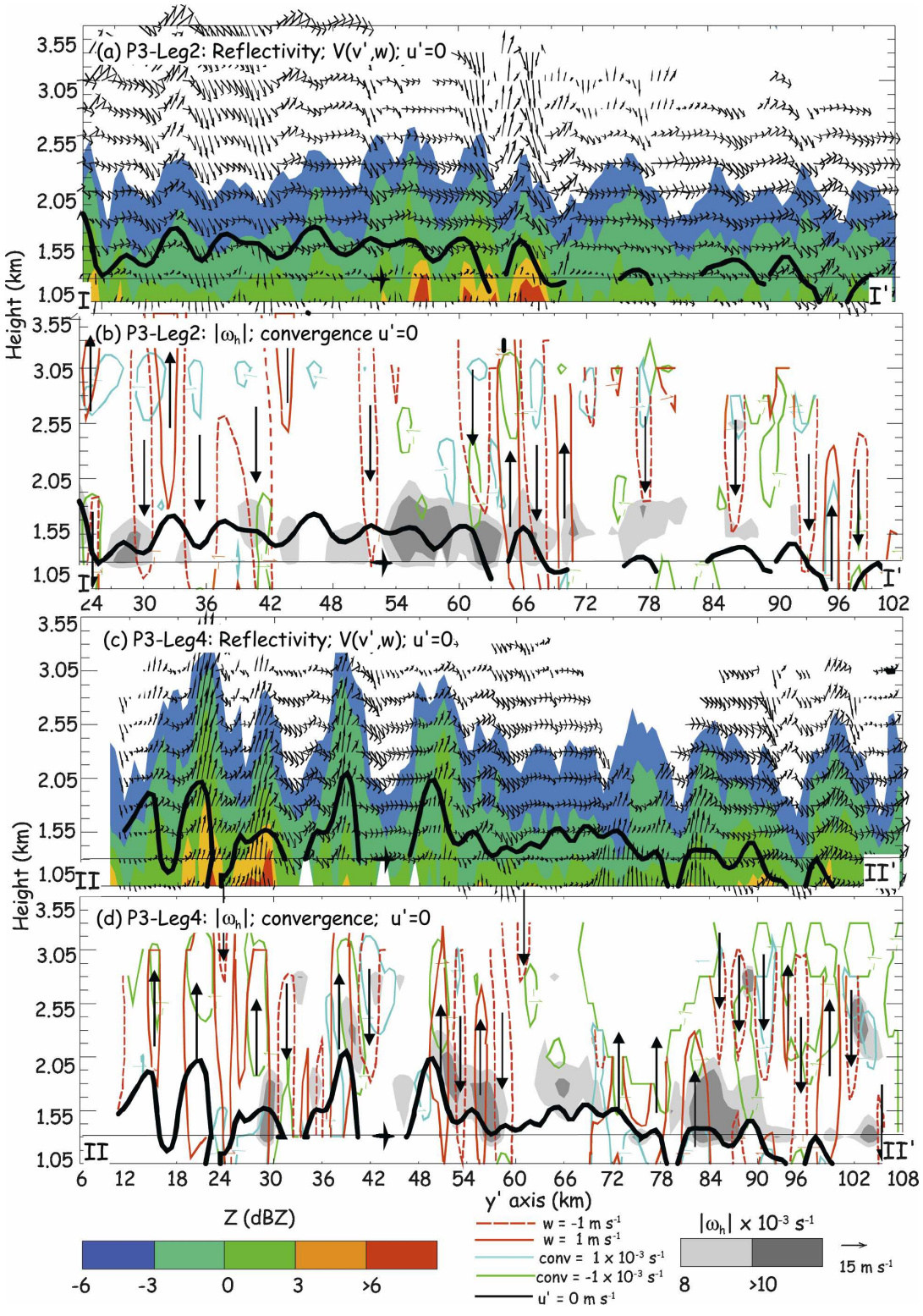

FIG. 14. Southwest–northeast vertical cross section within the postfrontal region during P3 (a), (b) leg 2 and (c), (d) leg 4. The location of the cross sections is indicated in Fig. 13a, labeled as (a), (b) I–I′, and in Fig. 13b, (c), (d) labeled as II–II′. (a), (c) Color-coded ELDORA reflectivity (scale at the bottom) overlaid by wind vectors (arrows with asymmetric scale indicated) in the plane of the cross section. (b), (d) Gray-shaded magnitude of horizontal vorticity (scale at the bottom), vertical velocity contours (red lines; see scale at the bottom), convergence contours (turquoise lines), and divergence contours (green lines). Updraft areas are indicated by red, solid lines and upward-pointing arrows; downdrafts are indicated by red, dashed lines and downward-pointing arrows. In all panels the kinematic boundary is indicated as a thick black line and the flight level at 1.3 km MSL as a horizontal, thin black line with the aircraft symbol.

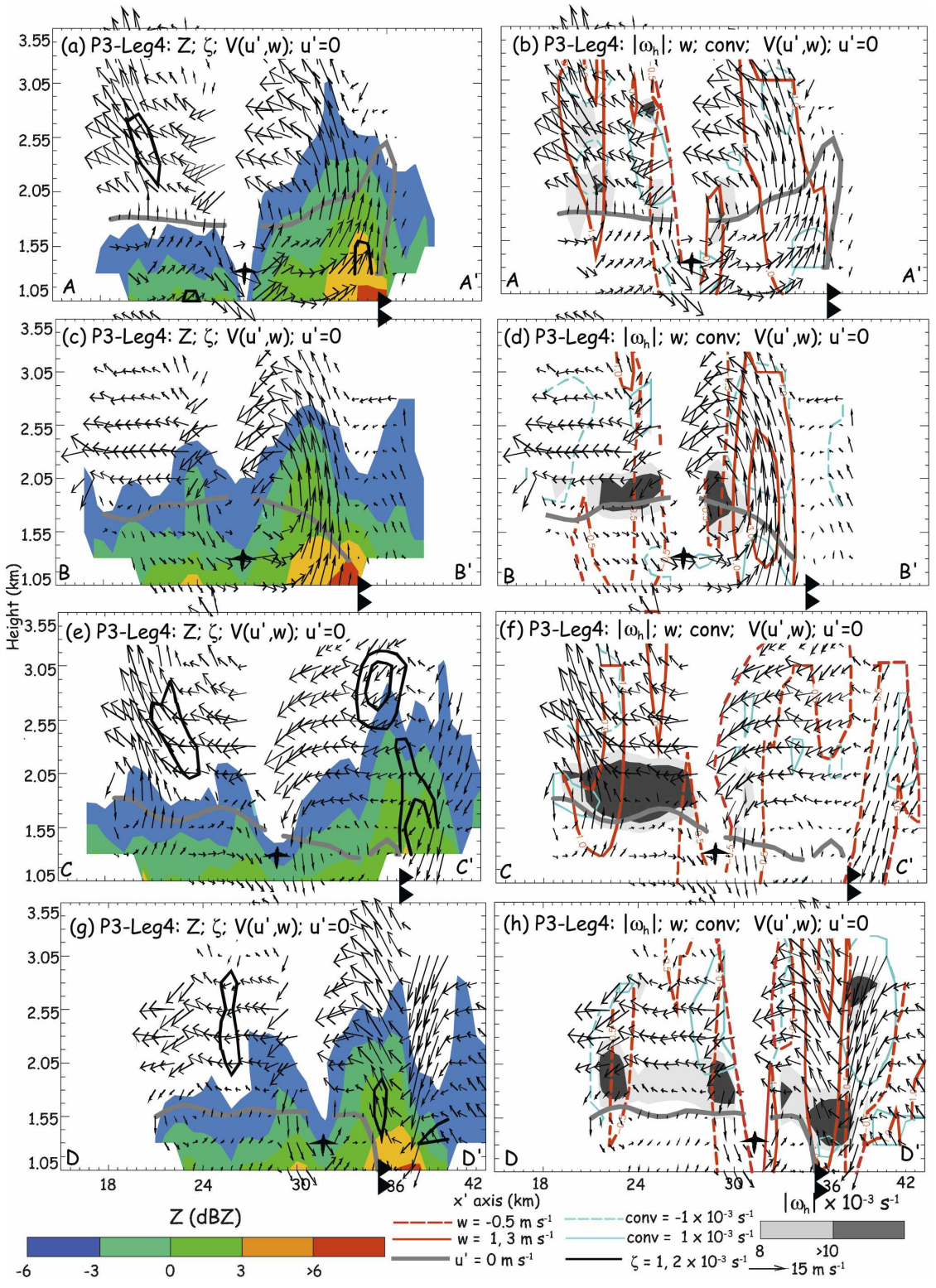

FIG. 15. Northwest–southeast vertical cross section for P3 leg 4 as indicated in Fig. 13b with (a) A–A′, (b) B–B′, (c) C–C′, and (d) D–D′. (left) Color-coded ELDORA reflectivity (scale at the bottom) overlaid by wind vectors (arrows with asymmetric scale indicated) in the plane of the cross section and vertical vorticity contours (thin black lines). (right) Gray-shaded magnitude of horizontal vorticity overlaid by vertical velocity contours (red lines) and convergence contours (turquoise lines). Upward motion and convergence are indicated by solid lines; downward motion and divergence are highlighted by dashed lines. In all panels the kinematic boundary is indicated as a thick gray line; the location of the flight path is shown by the aircraft symbol.

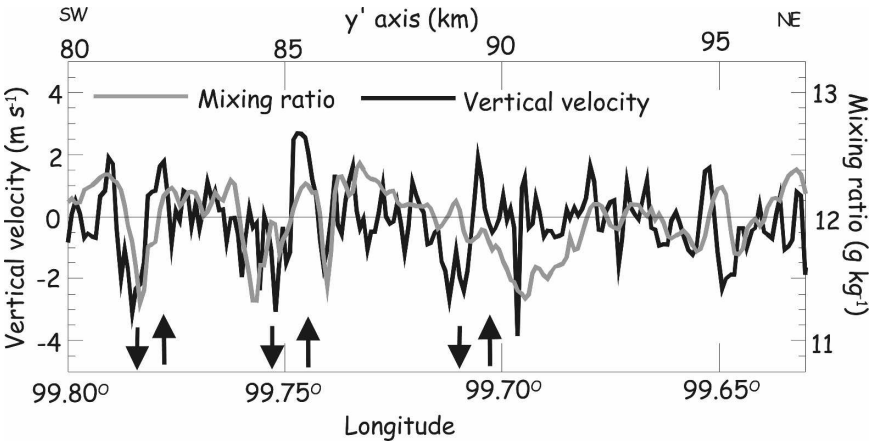

FIG. 16. Horizontal profile of vertical velocity (black line) and mixing ratio (gray line) at 1.3 km MSL within the postfrontal air measured between 2020 and 2023 UTC (P3 leg 6) by in situ instruments mounted on the P3 aircraft. Thick arrows indicate the probable location of Kelvin–Helmholtz waves.

for the existence of Kelvin–Helmholtz waves. Richardson numbers were derived from vertical profiles of temperature and wind measured by the dropsondes placed within the cool-air sector ~3–30 km from the leading edge (Figs. 2d,g; Table 2). The smallest Richardson numbers of 0.3–0.4 occurred between 1936 and 1939 UTC when the vortex lines were most distinct (Fig. 13b). They increased to 0.55–1.0 between 2051 and 2054 UTC when the vortex lines became more diffuse (Fig. 13c). Although the Richardson numbers were too large for the development of Kelvin–Helmholtz waves, they were sufficient to maintain these waves. The dropsondes were not well located and timed with respect to the occurrence of the waves, which were detected farther to the southwest between 1845 and 1945 UTC. Mueller and Carbone (1987) and Weckwerth and Wakimoto (1992) also observed Richardson numbers that were not sufficiently small to generate Kelvin–Helmholtz instabilities, although the main characteristics of the waves in their cases fit the Kelvin–Helmholtz theory.

Further evidence for Kelvin–Helmholtz waves is given by the evolution and the horizontal wavelength of the vortex lines. Droegemeier and Wilhelmson (1987) and Mueller and Carbone (1987) showed that Kelvin–Helmholtz waves form near the gust-front head and propagate on top of the boundary in time similar to what was observed on 10 June during P3 leg 2 and leg 4 (Figs. 12a,b). According to linear theory, Kelvin–Helmholtz waves should have a wavelength of 4.4–7.5 times the vertical thickness of the shear layer (Miles and Howard 1964; Mueller and Carbone 1987). Based on dropsonde data between 1936 and 2057 UTC, the depth of the shear layer was about 0.6–1.3 km (Table 2). The resulting wavelength according to linear theory would range between about 3 and 10 km. The separation of the horizontal vorticity maxima reveals a wavelength of about 6 km (Fig. 13b), which is about the mean value of the 3–10-km wavelength derived from linear theory. Although vertical velocity (Fig. 16) does not suggest a pronounced pattern, it can be hypothesized that three vortices rotating in a counterclockwise

TABLE 2. Parameters for calculating Richardson number (Ri), which is the ratio between stability to front-normal wind shear ($\partial u'/\partial z$). Stability is indicated by the Brunt–Väisälä frequency (N^2) with $N^2 = (g/\theta)(\Delta\theta/\Delta z)$, with g being the gravity acceleration (~9.8 m s^{-2}), θ being potential temperature, and Δz being the depth of the shear layer. Values were derived from dropsondes launched above the cool-air sector.

	1936 UTC	1939 UTC	2054 UTC	2057 UTC
Distance from the cold front leading edge (km)	30	5	3	28
Δz (m)	600	1300	700	1100
$\Delta\theta$ (K)	2.7	0.6	0.4	2.0
$\Delta u'$ (m s^{-1})	11.1	8.5	8.3	8.1
$N^2 \times 10^{-5}$ (s^{-2})	14	1.4	1.7	5.7
Ri	0.41	0.34	0.55	1.04

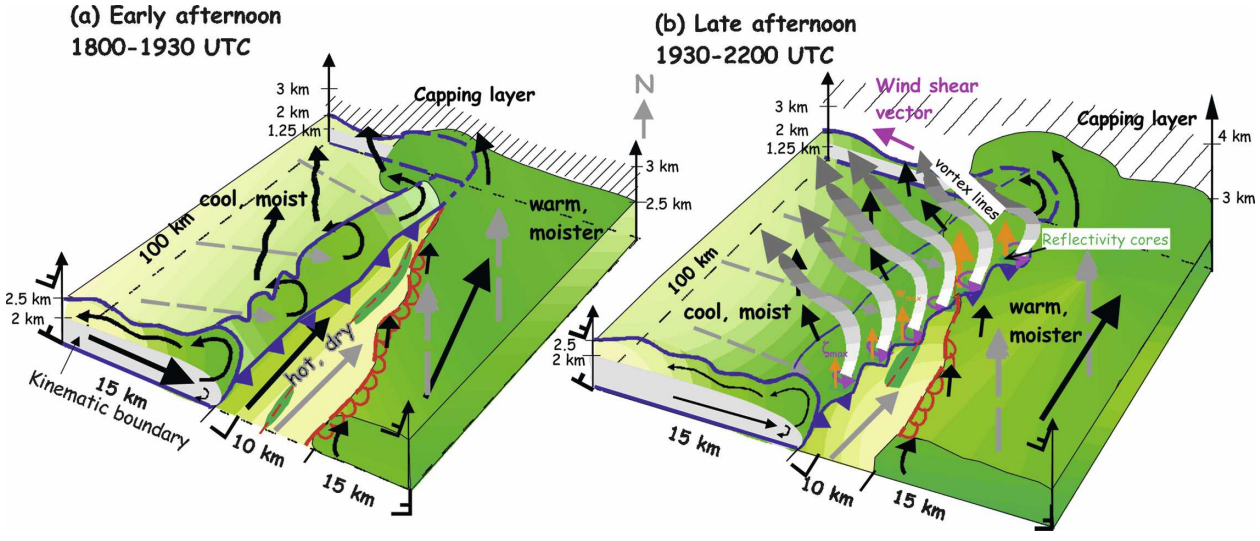

FIG. 17. Schematic diagram combining the results of this study with those achieved in Part I. The location of the surface cold front is shown as a blue line with alternating filled triangle symbols; the dryline is marked as a red line with semicircles attached; and the reflectivity thin line as a dashed red line. The kinematic boundary, defined as the zero across-front wind speed, is highlighted in gray. Wind vectors are indicated by black, solid arrows; magnitude of the wind vector is related to its thickness; dashed, gray lines indicate surface winds. Green shading is related to the moisture content; darker colors are related to higher moisture values. Areas of enhanced positive vertical vorticity are marked as purple circles with unidirectional arrow in (b); sizes of vertical vorticity symbols are scaled to their intensity. Updraft maxima are depicted by orange arrows; length is related to magnitude. Gray-shaded lines in (b) indicate schematically the location of vortex lines. More dense hatching for the capping layer corresponds to stronger stability.

direction with ~4–5-km spacing were observed (arrows in Fig. 16). The orientation of the wave crests is ~65° off the cold front leading edge and parallel to the wind shear vector (Fig. 13). While most studies have revealed waves parallel to the boundary (e.g., Droegemeier and Wilhelmson 1987; Mueller and Carbone 1987), Weckwerth and Wakimoto (1992) observed waves almost perpendicular (~70°) to the gust-front interface and concluded that the orientation is attributed to being parallel to the low-level wind shear vector.

Figure 13b indicates that some vortex lines are also connected to vertical vorticity maxima at the cold front leading edge. Weckwerth and Wakimoto (1992) observed a cold-air outflow boundary with hypothesized Kelvin–Helmholtz waves atop its upper interface with the environment and vertical vorticity maxima along its lateral interface with the environment, the gust-front leading edge. The horizontal vortex lines atop the boundary associated with the Kelvin–Helmholtz waves connected with the vertical vortex lines at the gust front. They hypothesized that the wave lines were tilted by the frontal updraft and subsequently stretched by the frontal convergence. This theory might be applicable to the present case as well because some of the lines are also connected to vertical vorticity maxima. Additionally, the analysis of the individual terms of the vorticity equations reveals that the time change is almost entirely a result of the tilting term (not shown).

6. Conclusions

The kinematic and thermodynamic structures of a nonprecipitating, slowly moving cold front observed in west-central Kansas on 10 June 2002 during IHOP were examined with airborne instrumentation that included Doppler radars, a differential absorption lidar, and in situ sensors. Intensive observations were collected along a 125-km segment of the front, allowing investigation of the spatial and temporal evolution of kinematic and thermodynamic structures in the vicinity of the cold front leading edge and the post- and prefrontal areas. The analysis also included vertical profiles of temperature, humidity, and wind from dropsondes deployed within the cool-air sector. In contrast to Part I, where across-front structures were emphasized, this investigation focused on structures observed in the alongfront dimension. A conceptual model of the conditions along the cold front on 10 June is presented in Fig. 17.

In the early afternoon (Fig. 17a; 1800–1930 UTC) the cold front was located in the northwestern part of the observational domain. Core and gap structures were evident in the southwestern part of the cold front leading edge, and weakly developed kinks in the reflectivity field were observed. The postfrontal sector was dominated by cool, moist air ($\theta_e \sim 350$ K, $\theta_v \sim 316$ K, $q \sim 11.5$–12.5 g kg^{-1}), with ~5 m s^{-1} surface winds from the

northwest backing to 10–15 m s^{-1} winds from south-southwest on top of the boundary (~2 km MSL). As shown in Part I, the cool-air sector showed gravity current characteristics such as a pronounced feeder flow toward the cold front leading edge, a rotor circulation at the leading edge, and a front-to-rear flow at the top of the cold outflow. The kinematic boundary height of the cold front ranged between 1 and 1.25 km MSL in the northeastern part and between 1.5 and 2.0 km in the southwestern part of the cold front.

An extension of the large-scale dryline located to the south was observed separating hot, dry air ($\theta_e \sim 348$ K, $\theta_v \sim 319$ K, $q \sim 9.5$–11 g kg^{-1}) advected from the southwest at ~7 m s^{-1} located immediately ahead of the cold front from warm, moister air ($\theta_e \sim 351$ K, $\theta_v \sim 317$ K, $q > 12$ g kg^{-1}) located farther to the southeast that was advected from the south at ~10 m s^{-1}. All three air masses were capped by a strong stable layer at about 2–2.5 km (Part I), indicated by the hatched area. The change in wind direction (~20–30°) was less distinct and updrafts were weaker (~0.5 m s^{-1}) at the dryline compared to the cold front (Part I). Within the hot, dry air mass, a reflectivity thin line parallel to the dryline that was located farther to the east was evident with reflectivities between 6 and 11 dB*Z*. The northeastern extent of the reflectivity thin line decayed or intersected the cold front between 1930 and 2000 UTC. Pronounced updrafts usually associated with intersecting boundaries were not observed. The dryline remained almost stationary in the southwestern part of the observational domain and was characterized by bulge-like eastward and westward displacements. Later in the early afternoon the northeastern part of the dryline and southern reflectivity thin line moved toward the cold font leading edge.

In the late afternoon (Fig. 17b; 1930–2200 UTC) horizontal wind shear at the cold front leading edge increased along the entire cold front with the approach of the dryline and reflectivity thin line, which served as a catalyst to trigger instabilities that intensified to misocyclones (purple circles in Fig. 17b). Organized patterns of misocyclones with a spacing of 5–8 km were observed between 1951 and 2005 UTC. Later in the afternoon, misocyclones still occurred, but without an organized pattern. When the frontal circulation weakened in the late afternoon because of diabatic heating (Part I), misocyclones had a greater influence on the organization of the vertical velocity than when the frontal circulation was stronger. The development of core-gap structures and kinks in the reflectivity field along the cold front on 10 June can be one manifestation of horizontal instabilities. At the same time misocyclones occurred at the cold front leading edge, zones of enhanced low-level convergence and enhanced updraft of >2 m s^{-1} (orange arrows) were observed. With an updraft of 2–4 m s^{-1} air parcels need to remain in the updraft for ~12–24 min in order to reach the level of free convection located at 3.8 km MSL (2.9 km AGL) at 2100 UTC (Part I). Enhanced updraft regions were observed along the cold front between 1930 and 2100 UTC. The position of the vertical velocity relative to the misocyclones is inconsistent; some vertical velocity maxima were on one side of the misocyclones, some were on both sides, while others were nearly collocated as also found by Friedrich et al. (2005).

Thermodynamic conditions became more favorable for convection initiation with increasing convective available potential energy, decreasing convective inhibition, a decrease of the level of free convection, and weakening of the capping layer in the later afternoon (Part I, Table 1). Convection along the cold front leading edge was first observed at 2125 UTC close to the area where the southwestern reflectivity thin line intersected the cold front at ~2015 UTC. Convection was also observed at about 2136 UTC in the northeastern part of the observational domain where the northeastern reflectivity thin line (~1930 UTC) and the dryline (~2015 UTC) intersected the cold front. Airborne instruments covering a wide along-frontal range were only available until 2041 UTC, so that the influence of wind shear instability on convection initiation remains speculative. Based on the kinematic structures observed prior to 2041 UTC it can be hypothesized that wind shear instabilities might favor convection initiation because vertical vorticity and vertical velocity maxima were primarily observed in the area where prefrontal boundaries intersected the cold front. It can be further assumed that the moisture necessary for cloud development was provided mainly by the approach of the warm, moister air in the northeastern part of the observing domain. Cloud development southwest of the dryline–cold front triple point might have been favored by the transport of moisture through the reflectivity thin line and that fact that the dry air was located mainly below 1.8 km. Mixing ratio at 1.3 km MSL and immediately ahead of the cold front increased from 10 to 12 g kg^{-1} between 1900 and 2041 UTC.

Organized structures manifested as horizontal vorticity maxima (vortex lines indicated as gray areas) were observed within the cool air in the late afternoon. These vortex lines developed at the cold front leading edge and were found ~20 km behind the cold front on top of the cold front boundary between 1929 and 1944 UTC. The lines were spaced at ~3–6-km intervals, oriented ~65° relative to the cold front leading edge, almost perpendicular to the boundary layer wind and al-

most parallel to the wind shear vector. It seems most likely that these features were forced by dynamical instabilities occurring between the cool air and the environment immediately above. The observational data do not unambiguously support the existence of either horizontal convective rolls or Kelvin–Helmholtz waves. Based on the ELDORA data, the vortex lines were not observed entirely within the boundary layer, which argues against horizontal convective rolls. Strong horizontal and vertical wind shear, short lifetime, and low Richardson numbers (~0.3 at 1939 UTC) are factors that support the argument for Kelvin–Helmholtz instabilities.

This case study showed that strong dynamical instabilities occurred at the interface between the slowly moving cold front and prefrontal boundaries, which could have been preferred regions of convection initiation. Measurements of high temporal and spatial resolution throughout the entire boundary layer are necessary to further investigate the influence of dynamical instabilities along slowly moving cold fronts and their influence on convection initiation. Future field experiments should also focus on high-resolution measurements ahead of the front, which are necessary to better understand formation, development, decay of the prefrontal boundaries, and their influence for convection initiation.

Acknowledgments. We extend special thanks to Yvette Richardson of The Pennsylvania State University and Tammy Weckwerth of NCAR for many fruitful discussions regarding this paper. Editing and interpolation of radar data were performed using the SOLO and REORDER programs. We thank the two anonymous reviewers for providing comments and suggestions that enhanced the quality of the paper. Dual-Doppler analyses were performed using the CEDRIC program. Huaqing Cai, Michael Bell, and Wen-Chau Lee of NCAR assisted in the installation and operation of the tuning-fork software to correct ELDORA data for navigation errors. Ming Xiao of DRI assisted with editing of radar data. This research was sponsored by the National Science Foundation under Grants ATM-9901688 and ATM-0432951 (Friedrich and Kingsmill) and ATM-021048 (Murphey and Wakimoto).

REFERENCES

Arnott, N. R., Y. P. Richardson, J. M. Wurman, and E. M. Rasmussen, 2006: Relationship between a weakening cold front, misocyclones, and cloud development on 10 June 2002 during IHOP. *Mon. Wea. Rev.,* **134,** 311–335.

Atkins, N. A., and R. M. Wakimoto, 1997: Influence of the synoptic-scale flow on sea breezes observed during CaPE. *Mon. Wea. Rev.,* **125,** 2112–2130.

Barcilon, A., and P. G. Drazin, 1972: Dust devil formation. *Geophys. Fluid Dyn.,* **4,** 147–158.

Barnes, S. L., 1973: Mesoscale objective map analysis using weighted time-series observations. NOAA/National Severe Storms Laboratory Tech. Memo. ERL NSSL-62, 60 pp.

Bluestein, H. B., and C. R. Parks, 1983: A synoptic and photographic climatology of low-precipitation severe thunderstorms in the southern plains. *Mon. Wea. Rev.,* **111,** 2034–2046.

——, E. W. McCaul, G. P. Byrd, R. L. Walko, and R. Davies-Jones, 1990: An observational study of convective clouds. *Mon. Wea. Rev.,* **118,** 1359–1370.

Bosart, B. L., W.-C. Lee, and R. M. Wakimoto, 2002: Procedures to improve the accuracy of airborne Doppler radar data. *J. Atmos. Oceanic Technol.,* **19,** 322–339.

Brown, R. A., 1980: Longitudinal instabilities and secondary flows in the planetary boundary layer: A review. *Rev. Geophys. Space Phys.,* **18,** 683–697.

Browning, K. A., and T. W. Harrold, 1970: Air motion and precipitation growth at a cold front. *Quart. J. Roy. Meteor. Soc.,* **96,** 369–389.

Bruneau, D., P. Quaglia, C. Flamant, M. Meissonnier, and J. Pelon, 2001: Airborne lidar LEANDRE II for water-vapor profiling in the troposphere. I. System description. *Appl. Opt.,* **40,** 3450–3461.

Buban, M. S., C. L. Ziegler, E. N. Rasmussen, and Y. R. Richardson, 2007: The dryline on 22 May 2002 during IHOP: Ground-radar and in situ data analysis of the dryline and boundary layer evolution. *Mon. Wea. Rev.,* **135,** 2473–2505.

Cai, H., W.-C. Lee, T. M. Weckwerth, C. Flamant, and H. V. Murphey, 2006: Observations of the 11 June dryline during IHOP_2002—A null case for convection initiation. *Mon. Wea. Rev.,* **134,** 336–354.

Carbone, R. E., 1982: A severe frontal rainband. Part I: Stormwide hydrodynamic structure. *J. Atmos. Sci.,* **39,** 258–279.

——, 1983: A severe frontal rainband. Part II: Tornado parent vortex circulation. *J. Atmos. Sci.,* **40,** 2639–2654.

——, M. J. Carpenter, and C. D. Burghart, 1985: Doppler radar sampling limitations in convective storms. *J. Atmos. Oceanic Technol.,* **2,** 357–361.

——, J. W. Conway, N. A. Crook, and M. W. Moncrieff, 1990: The generation and propagation of a nocturnal squall line. Part I: Observations and implications for mesoscale predictability. *Mon. Wea. Rev.,* **118,** 26–49.

Crawford, T. M., and H. B. Bluestein, 1997: Characteristics of dryline passage during COPS-91. *Mon. Wea. Rev.,* **125,** 463–477.

Cressman, G. P., 1959: An operational objective analysis system. *Mon. Wea. Rev.,* **87,** 367–374.

Crook, A. N., and M. W. Moncrieff, 1988: The effect of large-scale convergence on the generation and maintenance of deep moist convection. *J. Atmos. Sci.,* **45,** 3606–3624.

Demoz, B., C. Flamant, T. Weckwerth, D. Whiteman, K. Evans, F. Fabry, and P. Di Girolamo, 2006: The dryline on 22 May 2002 during IHOP_2002: Convective-scale measurements at the profiling site. *Mon. Wea. Rev.,* **134,** 294–310.

Droegemeier, K. K., and R. B. Wilhelmson, 1987: Numerical simulation of thunderstorm outflow dynamics. Part I: Outflow sensitivity experiments and turbulence dynamics. *J. Atmos. Sci.,* **44,** 1180–1210.

Ferrare, R. A., J. L. Schols, E. W. Eloranta, and R. Coulter, 1991: Lidar observations of banded convection during BLX83. *J. Appl. Meteor.,* **30,** 312–326.

Friedrich, K., D. E. Kingsmill, and C. R. Young, 2005: Misocyclone characteristics along Florida gust fronts during CaPE. *Mon. Wea. Rev.,* **133,** 3345–3367.

——, ——, C. Flamant, H. V. Murphey, and R. M. Wakimoto, 2008: Kinematic and moisture characteristics of a nonprecipitating cold front observed during IHOP. Part I: Acrossfront structures. *Mon. Wea. Rev.,* **136,** 147–172.

Geerts, B., R. Damiani, and S. Haimov, 2006: Finescale vertical structure of a cold front as revealed by an airborne Doppler radar. *Mon. Wea. Rev.,* **134,** 251–271.

Hane, C. E., C. L. Ziegler, and H. B. Bluestein, 1993: Investigation of the dryline and convective storms initiated along the dryline: Field experiments during COPS-91. *Bull. Amer. Meteor. Soc.,* **74,** 2133–2145.

——, M. E. Baldwin, H. B. Bluestein, T. M. Crawford, and R. M. Rauber, 2001: A case study of severe storm development along a dryline within a synoptically active environment. Part I: Dryline motion and an Eta Model forecast. *Mon. Wea. Rev.,* **129,** 2183–2204.

Hildebrand, H. P., C. A. Walther, C. L. Frush, J. Testud, and F. Baudin, 1994: The ELDORE/ASTRAIA airborne Doppler weather radar: Goals, design, and first field tests. *IEEE Proc.,* **82,** 1873–1890.

——, and Coauthors, 1996: The ELDORA/ASTRAIA airborne Doppler weather radar: High-resolution observations from TOGA COARE. *Bull. Amer. Meteor. Soc.,* **76,** 213–232.

Hobbs, P. V., and P. O. Persson, 1982: The mesoscale and microscale structure and organization of clouds and precipitation in midlatitude cyclones. Part V: The substructure of narrow cold-frontal rainbands. *J. Atmos. Sci.,* **39,** 280–295.

——, T. J. Matejka, P. H. Herzegh, J. D. Locatelli, and R. A. Houze Jr., 1980: The mesoscale and microscale structure and organization of clouds and precipitation in midlatitude cyclones. Part I: A case study of a cold front. *J. Atmos. Sci.,* **37,** 568–596.

Jorgensen, D. P., T. Matejka, and J. D. DuGranrut, 1996: Multibeam techniques for deriving wind fields from airborne Doppler radars. *J. Meteor. Atmos. Phys.,* **59,** 83–104.

——, Z. Pu, P. O. G. Persson, and W.-K. Tao, 2003: Variations associated with cores and gaps of a Pacific narrow cold frontal rainband. *Mon. Wea. Rev.,* **131,** 2705–2729.

Kingsmill, D. E., 1995: Convection initiation associated with a seabreeze front, a gust front, and their collision. *Mon. Wea. Rev.,* **123,** 2913–2933.

——, and N. A. Crook, 2003: An observational study of atmospheric bore formation from colliding density currents. *Mon. Wea. Rev.,* **131,** 2985–3002.

Lee, B. D., and R. B. Wilhelmson, 1997a: The numerical simulation of nonsupercell tornadogenesis. Part I: Initiation and evolution of pretornadic misocyclone circulations along a dry outflow boundary. *J. Atmos. Sci.,* **54,** 32–60.

——, and ——, 1997b: The numerical simulation of nonsupercell tornadogenesis. Part II: Evolution of a family of tornadoes along a weak outflow boundary. *J. Atmos. Sci.,* **54,** 2387–2415.

——, and ——, 2000: The numerical simulation of nonsupercell tornadogenesis. Part III: Parameter tests investigating the role of CAPE, vortex sheet strength, and boundary layer vertical shear. *J. Atmos. Sci.,* **57,** 2246–2261.

Lilly, D. K., 1966: On the instability of Ekman boundary flow. *J. Atmos. Sci.,* **23,** 481–494.

Locatelli, J. D., J. E. Martin, and P. V. Hobbs, 1995: Development and propagation of precipitation cores on cold fronts. *Atmos. Res.,* **38,** 177–206.

Marquis, J. N., Y. P. Richardson, and J. M. Wurman, 2007: Kinematic observations of misocyclones along boundaries during IHOP. *Mon. Wea. Rev.,* **135,** 1749–1768.

Matejka, T. J., R. A. Houze, and P. V. Hobbs, 1980: Microphysics and dynamics of the clouds associated with mesoscale rainbands in extratropical cyclones. *Quart. J. Roy. Meteor. Soc.,* **106,** 29–56.

Miles, J. W., and L. N. Howard, 1964: Note on heterogeneous shear flow. *J. Fluid Mech.,* **20,** 331–336.

Mueller, C. K., and R. E. Carbone, 1987: Dynamics of a thunderstorm outflow. *J. Atmos. Sci.,* **44,** 1879–1898.

Murphey, H. V., R. M. Wakimoto, C. Flamant, and D. E. Kingsmill, 2006: Dryline on 19 June 2002 during IHOP. Part I: Airborne Doppler and LEANDRE II analysis of the thin line structure and convection initiation. *Mon. Wea. Rev.,* **134,** 406–430.

Neiman, P. J., and R. M. Wakimoto, 1999: The interaction of a Pacific cold front with shallow air masses east of the Rocky Mountains. *Mon. Wea. Rev.,* **127,** 2102–2127.

O'Brien, J. J., 1970: Alternative solutions to the classical vertical velocity problem. *J. Appl. Meteor.,* **9,** 197–203.

Parsons, D. B., and P. V. Hobbs, 1983: The mesoscale and microscale structure and organization of clouds and precipitation in midlatitude cyclones. Part XI: Comparisons between observational and theoretical aspects of rainbands. *J. Atmos. Sci.,* **40,** 2377–2397.

——, M. A. Shapiro, R. M. Hardesty, R. J. Zamora, and J. M. Intrieri, 1991: The finescale structure of a west Texas dryline. *Mon. Wea. Rev.,* **119,** 1242–1258.

——, ——, and E. Miller, 2000: The mesoscale structure of a nocturnal dryline and of a frontal-dryline merger. *Mon. Wea. Rev.,* **128,** 3824–3838.

Pietrycha, A. E., and E. N. Rasmussen, 2004: Finescale surface observations of the dryline: A mobile mesonet perspective. *Wea. Forecasting,* **19,** 1075–1088.

Schaefer, J. T., 1986: The dryline. *Mesoscale Meteorology and Forecasting,* P. S. Ray, Ed., Amer. Meteor. Soc., 549–572.

Schultz, D. M., 2004: Cold fronts with and without prefrontal wind shifts in the Central United States. *Mon. Wea. Rev.,* **132,** 2040–2053.

Stensrud, D. J., and H. N. Shirer, 1988: Development of boundary layer rolls from dynamic instabilities. *J. Atmos. Sci.,* **45,** 1007–1019.

Wakimoto, R. M., and B. L. Bosart, 2000: Airborne radar observations of a cold front during FASTEX. *Mon. Wea. Rev.,* **128,** 2447–2470.

——, H. V. Murphey, E. V. Browell, and S. Ismail, 2006: The "Triple Point" on 24 May 2002 during IHOP. Part I: Airborne Doppler and LASE analyses of the frontal boundaries and convection initiation. *Mon. Wea. Rev.,* **134,** 231–250.

Weckwerth, T. M., and R. M. Wakimoto, 1992: The initiation and organization of convective cells atop a cold-air outflow boundary. *Mon. Wea. Rev.,* **120,** 2169–2187.

——, and D. B. Parsons, 2006: A review of convection initiation and motivation for IHOP-2002. *Mon. Wea. Rev.,* **134,** 5–22.

——, J. W. Wilson, R. M. Wakimoto, and N. A. Crook, 1997: Horizontal convective rolls: Determining the environmental conditions supporting their existence and characteristics. *Mon. Wea. Rev.,* **125,** 505–526.

——, and Coauthors, 2004: An overview of the International H_2O Project (IHOP_2002) and some preliminary highlights. *Bull. Amer. Meteor. Soc.,* **85,** 253–277.

Weiss, C. C., and H. B. Bluestein, 2002: Airborne pseudo-dual Doppler analysis of a dryline-outflow boundary intersection. *Mon. Wea. Rev.,* **130,** 1207–1226.

——, ——, and A. L. Pazmany, 2006: Finescale radar observations of the 22 May 2002 dryline during the International H_2O Project (IHOP). *Mon. Wea. Rev.,* **134,** 273–293.

Wilson, J. W., and R. D. Roberts, 2006: Summary of convective storm initiation and evolution during IHOP: Observational and modeling perspective. *Mon. Wea. Rev.,* **134,** 23–47.

——, G. B. Foote, N. A. Crook, J. C. Fankhauser, C. G. Wade, J. D. Tuttle, C. K. Mueller, and S. K. Krueger, 1992: The role of boundary-layer convergence zones and horizontal rolls in the initiation of thunderstorms: A case study. *Mon. Wea. Rev.,* **120,** 1785–1815.

Young, G. S., and R. H. Johnson, 1984: Meso- and microscale features of a Colorado cold front. *J. Appl. Meteor.,* **23,** 1315–1325.

Ziegler, C. L., E. N. Rasmussen, M. S. Buban, Y. P. Richardson, L. J. Miller, and R. M. Rabin, 2007: The "Triple point" on 24 May 2002 during IHOP. Part II: Ground-radar and in situ boundary layer analysis of cumulus development and convection initiation. *Mon. Wea. Rev.,* **135,** 2443–2472.